AIChE

Microscopic Imaging of Biphasic Oil-Air Flow in French Fries Using Synchrotron Radiation

Anna Patsioura
INRA, UMR 1145 Ingénierie Procédés Alimentaires, Interaction between Materials and Media in Contact group,
F-91300 Massy, France

AgroParisTech, UMR 1145 Ingénierie Procédés Alimentaires, F-91300 Massy, France

Jean-Michaël Vauvre
INRA, UMR 1145 Ingénierie Procédés Alimentaires, Interaction between Materials and Media in Contact group,
F-91300 Massy, France

AgroParisTech, UMR 1145 Ingénierie Procédés Alimentaires, F-91300 Massy, France

McCain Alimentaire S.A.S., Parc d'entreprises de la Motte du Bois, 62440 Harnes, France

Régis Kesteloot
Régis Kesteloot conseil, 60 Avenue du Colonel Driant, 59130 Lambersart, France

Frédéric Jamme
Synchrotron SOLEIL, L'orme des Merisiers Saint-Aubin, BP 48, 91192 Gif-sur-Yvette cedex, France

Pamela Hume
McCain Foods Ltd., Havers Hill, Scarborough YO113BS, U. K.

Olivier Vitrac
INRA, UMR 1145 Ingénierie Procédés Alimentaires, Interaction between Materials and Media in Contact group,
F-91300 Massy, France

AgroParisTech, UMR 1145 Ingénierie Procédés Alimentaires, F-91300 Massy, France

DOI 10.1002/aic.14744

Spontaneous oil percolation in French fries was studied dynamically at cellular scale using deep-UV synchrotron radiation enabling to image simultaneously the fluorescence of cell walls and of dyed oil. Experimental results report 75 oil filling kinetics of potato parenchyma cells previously emptied and equilibrated with superheated steam in conditions mimicking immersion frying. Counter-current oil-air flow was found the dominant factor controlling the kinetic of oil penetration, whereas, trapped bubbles delay the passage of oil from the first to the second cell layer for additional several minutes. The frequency of occurrence of passages between layers was assessed much lower than the percolation threshold suggested by the hierarchical honeycomb arrangement of cells. A description relating microscopic oil-air flow and oil uptake is detailed in a companion paper. © 2015 American Institute of Chemical Engineers *AIChE J*, 61: 1427–1446, 2015
Keywords: deep-fat frying, oil, spontaneous imbibition, synchrotron radiation, mass transfer, food

Introduction

Deep-fat frying is an important multifunctional food process unit operation, which consists in immersing a wet product in a liquid with a high boiling point such as edible oil or fat.[1] It induces rapid food cooking and drying.[2,3] As a significant oil pickup is also observed, fried products suffer globally a poor image in western countries.[4] From an industrial point of view, the possibility to reduce oil uptake could change the perspective and stimulate new deep fryer designs. As reviewed in,[1,5] it offers indeed the fastest heat-transfer coefficients among all conventional cooking and drying food operation units, with values up to 2 kW m^{-2} K^{-1}.[6–8] When combined with temperatures from 160 to 180°C, high vaporization rates generate sufficient steam pressure loss through the crust to oppose any oil penetration by capillarity.[9,10] Oil pickup occurs consequently mainly when the product is removed from the frying bath.[11,12] Oil adheres to the product surface and penetrates the crust either by spontaneous imbibition[9,10] or driven by the inner condensation of steam.[13,14]

The general intent of this study is to visualize the oil uptake mechanisms in potato parenchyma tissues and to understand how oil penetration may be hampered by the presence of an incondensable phase during postfrying. At

---

Correspondence concerning this article should be addressed to O. Vitrac at olivier.vitrac@agroparistech.fr.

this stage, the product crust—which is in contact both with oil and air—passes in few seconds from an ambiance containing saturated steam at 120°C or above, to a colder one at 100°C or below. It is indeed thought that the pressure recovery inside the product after cooling would be related to a competition between oil and air penetration. Recent experiments on glass microchannels[15] mimicking cell connections confirmed this description. The microscopic observations reported in this study provide ground of a general micromodel of oil-air menisci displacements in real tissues as detailed in.[16] Comparatively to previous models,[17–20] it would enable to simulate numerically the oil barrier effects created by the arrangements of cells, cell walls, and starch. These developments are particularly essential to elucidate why oil is mainly located within the first two cell layers when French fries are prepared from fresh potatoes[21] whereas it can reach core regions in parfried frozen French fries.[22]

The article is organized as follows. Theory Section introduces the thermodynamics of steam in equilibrium with the hygroscopic product crust. These concepts justify our substitution of the initial frying step by an equilibration step in superheated steam (SHS). Materials and Methods Section details the studied materials and the conditions of dynamic observations of oil-air biphasic flows in parenchyma tissues mimicking the crust of a potato strip. Starch content was removed to study specifically the effect of cell arrangements and cell defects on oil percolation. Our *in situ* imaging methodology combined a deep ultraviolet synchrotron source and a photo-amplified Charged Coupled Device (CCD) camera to collect simultaneously the fluorescence of cell walls and of dyed oil at the scale of about 1 µm. A devoted image analysis software has been developed to separate the dense phases and their spatial arrangements. Results and Discussion Section presents the percolation kinetics during postfrying at the scales of a centimeter scale tissue to get reliable statistics and at the scale of individual cells to gain access to percolation mechanisms. The conclusions and their extrapolations to real process conditions are finally discussed in Conclusion Section.

Theory

Beyond early phenomenological descriptions,[23] several successful models have been proposed to predict coupled heat and mass transfer during frying. They include descriptions of frying as moving vaporization front[24–26] or as coupled set of heat- and mass-transfer equations in porous media with phase change.[17–19,27,28] Such models are considered enough accurate to simulate reactions[27,29] and texture modifications in deep-fat fried products.[30] Oil uptake is by contrast less extensively described. Reviews on oil uptake update regularly the mechanistic findings.[31–34] The generally accepted mechanisms are derived from enlightening experiments involving successive frying in nondyed and dyed oils[9] or surface oil washing.[10]

Overpressure prevents oil uptake during immersion frying

During deep frying, the fried product evolves rapidly to a composite material comprising a dried crust sandwiching a rich-in-water internal compartment.[17,24,35] The vaporization region is located at the crust-core interface with an exact position fluctuating with capillary migration of liquid water.[2] Though the dried crust is highly wettable by oil, it is usually thought that internal pressure rise, which can reach 35 kPa in French fry type products,[13,36] opposes to oil capillary pressure during the immersion stage.

The assumption of no oil pickup during immersion stage can be assessed from the geometry of defects enabling oil penetration in potato products: cut cells, damaged cell junctions, or cell walls.[21] By considering that oil passages are idealized as converging circular tubes, with a diverging angle ϕ ($\phi=0$ for open cells and $\phi > 0$ for defects between cells), the capillary pressure, denoted p_C, is given by (see Eq. 2.3.1 in[37] or Eq. 8.148 in[38])

$$p_c=\frac{4\gamma}{d}\cos\left(\theta_c-\phi\right) \tag{1}$$

where d is the defect diameter at the contact line. Oil wetting conditions of the crust at 120°C (see[39,40]) correspond to an oil-steam surface tension $\gamma=2.35\times10^{-2}\mathrm{N\ m^{-1}}$ and a contact angle $\theta_c=0.66$ rad.

For cylindrical capillaries ($\phi=0$), time-averaged internal positive pressure gauges reported in[13] (10 and 2 kPa, respectively, in starchy and rich-water gels) are overcome for diameters smaller than 17 and 87 µm, correspondingly. For converging capillaries verifying $\theta_C=\phi$, the critical openings are increased up to 22 and 111 µm, respectively. In comparison, potato parenchyma cells exhibit much larger diameters ranging from 150 to 300 µm.[41] Oil invasion via empty cells appears, therefore, very unlikely while a residual pressure drop exists across the crust. In potato strips, this condition is met everywhere except on edges.

Properties of steam in the crust during frying and post frying

During the whole immersion stage, the crust remains exposed to pure steam at a temperature above the boiling point of free water, denoted T_{sat}. Above T_{sat}, the hygroscopic properties of the matrix (starch, cellulose, and pectins) enforce that in absence of incondensable phase (air) the residual water content and the local crust temperature are negatively correlated: the increase of one parameter causes a the decreases of the other.[27] Once the product is removed from the frying bath, the equilibrium curves are displaced by the volume fraction of air incorporated. According to cooling or air filling effects are dominating, steam condensation (even above T_{sat}) or drying can occur and alter the evolution of gas pressure inside the cells. Practical relationships to define equivalent frying and postfrying conditions are presented here. In this study, we focused on conditions where oil uptake occurs only due to spontaneous imbibition (i.e., without steam condensation).

Properties of Air-Steam Mixtures in Isobaric Conditions. By assuming that steam is an ideal gas and that the activity of the vapor in equilibrium with the solid phase can be approximated from its partial pressure, P_v,[42] one gets the isobaric conditions of equilibrium of the crust with the surrounding gas

$$a_w(P,T)=\frac{f_v(P,T)}{f_v^{sat}(P,T)}\approx\frac{P_v(P)}{P_v{}^{sat}(T)}=x_v\frac{P}{P_v{}^{sat}(T)} \tag{2}$$

where x_v is the water vapor fraction; f_v and f_v^{sat} are the fugacities of water vapor and pure water, respectively. During immersion frying at constant pressure, $x_v=1$ and the decrease in water activity in the product is related to the sole increase in saturation pressure, P_v^{sat}, with temperature, T. The Clausius–Clapeyron relationship yields

$$\frac{d\left(\ln\left(P_{\mathrm{v}}^{\mathrm{sat}}\right)\right)}{d\left({}^{1}/_{T}\right)}=-\frac{\Delta H_{\mathrm{vap}}}{R} \tag{3}$$

with ΔH_{vap} the molar latent heat of vaporization of water and R the ideal gas constant.

Condensation of Steam During Cooling. During post frying, the equilibrium is displaced by subsequent cooling and air incorporation. From Eq. 2, both contributions have antagonist effects on gas pressure. Cooling by radiative and convective heat transfer was shown to provoke vacuums as low as 30–35 kPa in starchy fried products.[13,36] Isothermal mixing of steam with air causes alternatively sharp drop in relative humidity and subsequent crust drying.

The gas pressure evolution at cell scale between an initial (1) and final state (2) can be inferred from the mass balance between the gas-phase filling voids and cellular constituents. Each state is governed by four intensive quantities $\{P_i, T_i, x_{\mathrm{v}i}, X_i\}_{i=1,2}$, where $\{X_i\}_{i=1,2}$ is the residual amount of water respectively to the solid phase (nonfat). To keep derivations simple, air coming from the surroundings is assumed to replace or dilute water vapor but no water is exchanged with the surroundings. The variation of the water content reads accordingly

$$\Delta X=X_2-X_1=f(P_2,T_2,x_{\mathrm{v}2})-f(P_1,T_1,x_{\mathrm{v}1}) \tag{4}$$

where $f(P_i,T_i,x_{\mathrm{v}i})$ is the water sorption isotherm at temperature T_i giving the relationship between the residual water content in the solid phase in function of the water activity in the gas phase at equilibrium $a_{\mathrm{w}}(P_i,T_i,x_{\mathrm{v}i})$. The variation of total pressure on the gas phase between steps 1 and 2 within a cell is finally related to two contributions: a contraction of the gas proportional to T_1/T_2 and the condensation of water molecules initially in the gas phase, both effects lead to

$$P_2\mathrm{x}_{\mathrm{v}2}=\frac{T_2}{T_1}P_1\mathrm{x}_{\mathrm{v}1}-\rho_s\frac{1-\varepsilon}{\varepsilon}\frac{RT_2}{M_{\mathrm{w}}}\Delta X \tag{5}$$

where ρ_{S} is the density of the solid phase and M_{w} is the molecular weight of water.

Equation 4 shows that P_2 is proportional to the reciprocal volume fraction of steam in the crust. Equivalent fried (1) and postfried (2) states at atmospheric pressure ($P_1=P_2=P_{\mathrm{atm}}$) are achievable by choosing $T_2\approx T_1>T_{\mathrm{sat}}$, $x_{\mathrm{v}1}=1$ (equilibrium with SHS) and $x_{\mathrm{v}2}\rightarrow 0$ (contact with dry air). Choosing moderate temperatures close or below the glass transition temperature of cellular constituents minimize the risks of additional shrinkage due to drying.

Role of the Hygroscopic Behavior of the Matrix. By neglecting the effect of pressure on water sorption isotherms, Eqs. 4 and 5 become

$$P_2=\frac{1}{\mathrm{x}_{\mathrm{v}2}}\frac{T_2}{T_1}P_{\mathrm{atm}}-\rho_{\mathrm{s}}\frac{1-\varepsilon}{\varepsilon}\frac{RT_2}{\mathrm{x}_{\mathrm{v}2}M_{\mathrm{w}}}\left(f(T_2,x_{\mathrm{v}2})-f(T_1,1)\right) \tag{6}$$

The curve generated by the successive intersections of $f(T_i,\mathrm{x}_{\mathrm{v}i})$ with $a_{\mathrm{w}}(P_{\mathrm{atm}},T_i,1)$ is called sorption/desorption isobar.[43,44] Its general equation can be derived from the analytical expression of standard isotherms for hygroscopic products. We adopt here the Guggenheim-Anderson-de Boer (GAB) isotherm[45–47] as a general prototype of multilayer sorption isotherms

$$\begin{cases} X(T,x_{\mathrm{v}})=f(T,x_{\mathrm{v}}) \\ =X_{\mathrm{m}}\dfrac{C_{\mathrm{g}}(T)K(T)a_{\mathrm{w}}(T,x_{\mathrm{v}})}{\left(1-K(T)a_{\mathrm{w}}(T,x_{\mathrm{v}})\right)\cdot\left(1-K(T)a_{\mathrm{w}}(T,x_{\mathrm{v}})+C_{\mathrm{g}}(T)K(T)a_{\mathrm{w}}(T,x_{\mathrm{v}})\right)} \\ C_{\mathrm{g}}(T)=C_{\mathrm{g}0}\exp\left(\dfrac{\Delta H_C}{RT}\right) \\ K(T)=K_0\exp\left(\dfrac{\Delta H_K}{RT}\right) \end{cases} \tag{7}$$

where $\Delta H_C+\Delta H_K$ is the total net sorption energy due to the monolayer and multilayer.[48] $C_{\mathrm{g}0}$ and K_0 are preexponential factors. C_{g} is the ratio of the partition function between the monolayer and the multilayer.

Continuous medium approximation of oil transport in the product

Early descriptions of oil uptake found apparent correlations between water loss during frying and oil uptake.[26,49–51] They may be interpreted as the consequence of the creation of voids, which are subsequently filled with oil during cooling. Only a few mechanistic models of oil uptake have been proposed so far and its representation remains an open question in food materials with cellular structures.

Miscible Formulation Based on Linear Diffusion-Advection Equations. The first consistent description of oil uptake covering continuously frying and postfrying stages was proposed by Halder et al.[18] The model influenced by the abundant literature on flow and transport in fractured porous media assumes miscible flows (between oil, water, steam and air). The oil mass balance on an elementary representative volume is written as the consequence of a Darcy flow due to a total pressure gradient and of a capillary flow controlled by an effective diffusion coefficient, $D_{\mathrm{o,cap}}^{(T,S_{\mathrm{o}})}$

$$\frac{\partial}{\partial t}\left(\varepsilon\rho_{\mathrm{o}}{}^{(T)}S_{\mathrm{o}}\right)+\nabla\cdot\left(u_{\mathrm{o}}\rho_{\mathrm{o}}{}^{(T)}\right)=\nabla\cdot\left[D_{\mathrm{o,cap}}^{(T,S_o)}\nabla\left(\varepsilon\rho_{\mathrm{o}}{}^{(T)}S_{\mathrm{o}}\right)\right] \tag{8}$$

where S_{o} is the oil saturation (extent to which oil fills the pores), ρ_{o} is the intrinsic oil density. The volume averaged oil velocity u_{o} was given by the generalized Darcy's law

$$u_{\mathrm{o}}=-\frac{k_{\mathrm{in,o}}^{p}k_{\mathrm{r,o}}^{p}}{\mu_{\mathrm{o}}}\nabla P \tag{9}$$

whereas $D_{\mathrm{o,cap}}^{(T,S_{\mathrm{o}})}$ was formally defined as:

$$D_{\mathrm{o,cap}}^{(T,S_{\mathrm{o}})}=-\frac{k_{\mathrm{in,o}}^{p}k_{\mathrm{r,o}}^{p}{}^{(T,S_{\mathrm{o}})}}{\varepsilon\mu_{o}{}^{(T)}}\left.\frac{\partial p_{\mathrm{cap}}(S_{\mathrm{o}})}{\partial S_{\mathrm{o}}}\right|_{T} \tag{10}$$

$k_{\mathrm{in,o}}^{p}$ and $k_{\mathrm{r,o}}^{p}$ appearing in Eqs. 9 and 10 are the intrinsic permeability of the porous structure and its relative permeability to oil with respect to other fluid phases in the material (liquid water, water vapor, air), respectively.

The concept of relative permeability has been proposed first by Muskat and Meres[52] and is interpreted as the effect of phase distribution on viscous drag. Contrary to gases (see e.g., [53–55]), the determination of relative permeabilities to liquids is highly sensitive to the distribution of menisci and on the presence of trapped gas.[38] Due to the different inherent complications, an empirical model, independent of temperature, was instead applied by the authors, based on an early suggestion of[17]

$$D_{\mathrm{o,cap}}^{(S_o)}=D_{\mathrm{o}}\exp\left(-2.8+2.0\frac{\varepsilon}{1-\varepsilon}\frac{\rho_{\mathrm{o}}}{\rho_{\mathrm{s}}}S_{\mathrm{o}}\right) \tag{11}$$

where ρ_s is the intrinsic density of solid matrix.

The practical consequence of this miscible formulation is that the problem of oil uptake is dominated by diffusion and exhibit poor contrast behavior between immersion stage and cooling.[28] The values of the pre-exponential factor D_o, reported in[18,56] ranging from $1.22 \times \cdot 10^{-9}$ to $1.22 \times \cdot 10^{-7}$ $m^2\ s^{-1}$, lead oil to penetrate on distances from few millimeters up to centimeters. These values are unrealistic in potato tissues where oil remains mainly in superficial cells.[21]

Diffusion-Free Formulation Assuming an Oil-Gas Immiscible Flow. Immiscible flows (here oil and mixture of water vapor and air) are preferably described via the simplified continuity and momentum equations proposed by Bucklet and Leverett[57] or their evolutions.[37,38] When relative permeabilities do not vary significantly with S_o, the variation of the position, z, of the oil isosaturation lines obeys to a simple equation:

$$\left.\frac{dz}{dt}\right|_{S_{\mathrm{o}}}=\frac{\langle u_t\rangle}{\varepsilon}\frac{df_{\mathrm{o}}}{dS_{\mathrm{o}}} \tag{12}$$

where f_o is the relative volumetric oil flow rate and $\langle u_t \rangle$ is the total local superficial (Darcy) velocity averaged on a representative elementary volume of the crust. By neglecting the weight of the air column and buoyancy forces, one gets

$$\langle u_{\mathrm{t}}\rangle=\langle u_{\mathrm{o}}\rangle+\langle u_{\mathrm{g}}\rangle=-\frac{k_{\mathrm{in}}^{p}k_{\mathrm{r,o}}^{p}}{\mu_{\mathrm{o}}}\left(\frac{\partial p_{\mathrm{o}}}{\partial z}+\rho_{\mathrm{o}}g\sin\left(\theta_{\mathrm{u}}\right)\right)-\frac{k_{\mathrm{in}}^{p}k_{\mathrm{r,g}}^{p}}{\mu_{\mathrm{g}}}\left(\frac{\partial p_{\mathrm{g}}}{\partial z}\right) \tag{13}$$

where $\langle u_o \rangle$ and $\langle u_g \rangle$ are the local velocities of oil and gas, respectively, and θ_u is the polar angle measured from the horizontal plane with $\theta_u=\pi/2$ corresponding to positive velocities pointing against the gravity vector. By considering that oil is the wetting phase in oil-gas systems, capillary pressure is defined as the excess pressure seen by the non-wetting phase (gas) $p_c=p_g-p_o$. In fried products, superficial velocity is controlled by the superposition of two driving forces: the gradient of capillary forces and the gradient of gas pressure as measured by[13,36]

$$\langle u_{\mathrm{t}}\rangle=\frac{k_{\mathrm{in}}^{p}k_{\mathrm{r,o}}^{p}}{\mu_{\mathrm{o}}}\frac{\partial p_{\mathrm{c}}}{\partial z}-\left(\frac{k_{\mathrm{in}}^{p}k_{\mathrm{r,o}}^{p}}{\mu_{\mathrm{o}}}+\frac{k_{\mathrm{in}}^{p}k_{\mathrm{r,g}}^{p}}{\mu_{\mathrm{g}}}\right)\frac{\partial p_{\mathrm{g}}}{\partial z}-k_{\mathrm{in}}^{p}g\sin\left(\theta_{\mathrm{u}}\right)\left(\frac{k_{\mathrm{r,o}}^{p}}{\mu_{\mathrm{o}}}\rho_0\right) \tag{14}$$

Three limiting cases are particularly meaningful[58]

- spontaneous imbibition of oil when (e.g. no steam condensation);
- gas-oil cocurrent flow in direction z, when when air is "pushed" or "pulled" in the same direction (e.g. case of steam condensation);
- gas-oil counter-current flow, when due to (e.g. air is displaced by oil and compressed inside the sample).

In this diffusion-free formulation, the lowest oil invasion is obtained when the oil and gas flows are counter-current and when an internal overpressure exists. This possibility was reported by He et al.[14] Slow penetration rates are expected when air compensates partly or fully steam after frying. In absence of pressure drop, wicking experiments of[59] confirmed recently this description. This study replacing completely steam by air provides additional clues to justify an immiscible formulation instead of miscible one.[16]

Materials and Methods

Two cells thick potato tissue without starch

Parenchyma tissue of Potatoes of *Solanum tuberosum* L. cv. Bintje variety was used as model cellular material. Fresh potato tubers of 20 ± 3% dry matter (wet basis) were stored at 4°C at a relative humidity close to 95%. The central medulla was sliced with a microtome equipped with a binocular (model 2218 historange microtome, LKB, Bromma, Sweden) along the transversal axis of elongation. The quality of each cut was carefully tested under the microscope and its thickness checked with a thickness gauge to assess that the cells of each layer were separated by one single cell wall. Potato slices of a little less than two cell layers were grouped in two categories according to their thickness: (1) slices of 100–150 μm and (2) slices of 200–300 μm. The consequence was that starch granules could be easily removed from each opening by washing the tissue three times with cold water at 15°C. Microscopic observation in polarized light confirmed the absence of starch.

Dyed oils

The industrial blend of oils (80% of sunflower oil and 20% of high oleic sunflower oil) was supplied by McCain (Harne's plant, France). The composition in saturated, monosaturated and polysaturated fatty acids was 48, 40, and 12%, respectively. The iodine value was of 120 g iodine·100 g^{-1} oil.

Oil blend was stained with Sudan Red (CAS 1229-55-6, supplier Sigma Aldrich, Germany) at 1000 ppm for permeation experiments and dyed with a thermostable fluorescent probe (1,6-diphenyl-1,3,5-hexatriene, CAS 1720-32-7, supplier Sigma Aldrich, Germany) at 1000 ppm for dynamic imaging ones.

Equilibration of parenchyma cell walls with superheated steam

Superheated steam (SHS) was used to reproduce the thermodynamic conditions met in the crust of French fries during frying. This drying process mimics the par-frying process of industrial French fries with no oil contact. SHS was produced by a steam generator delivering 1400 kg s^{-1} of pure steam at 10 bars and 180°C, which was subsequently expended down to 3 bars and then to atmospheric pressure at 100°C. Steam temperature was finally overheated to any set temperature between 102°C and 180°C. Samples (thin slices) were equilibrated inside a 5 L thermoisolated chamber, where SHS at the desired temperature was circulating downwards. At the reference temperature of 120°C, the SHS

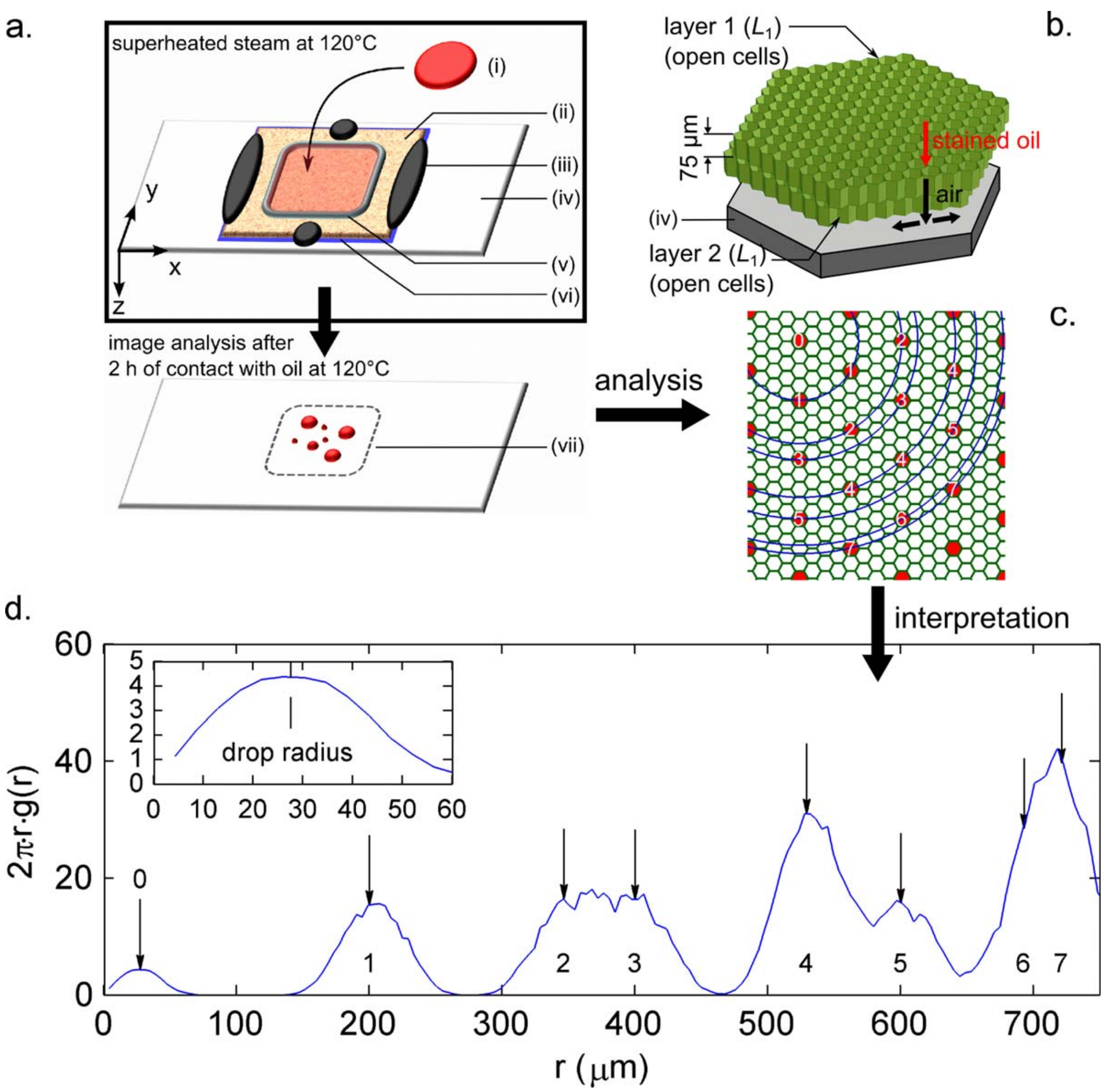

Figure 1. Oil breakthrough experiments on two cell layer potato tissues in thermodynamical conditions mimicking postfrying: (a) experimental setup, (b) details, (c) example of analysis assuming periodic spills, and (d) corresponding radial distributions functions assuming symmetric boundary conditions.

(1) Stained oil (Sudan Red), (2) potato crust, (3) adhesive, (4) glassy support, (5) adhesive, (6) porous spacer, and (7) oil spots. The numbers and arrows in (d) interpret the radial distributions based on an analysis centered on cell 0 in (c). Cells with the same number are at the same distance to the central one (0). [Color figure can be viewed in the online issue, which is available at wileyonlinelibrary.com.]

flow rate was of 0.68 $\mathrm{m}^3\ \mathrm{s}^{-1}$. The equilibrium condition was detected when the temperature differences, measured by two T-thermocouples located outside and at the center of a control slice, was lower than 0.50°C at 120°C. Equilibrium was usually reached after 2–4 h. Residual water content in equilibrated samples was determined after convective drying at 105°C until constant weight. Equilibrations were triplicated. For oil uptake dynamic observation, samples were equilibrated at 120°C and stored accordingly at 25°C and 50% of relative humidity.

Distribution and size of cell defects between two cell layers using a breakthrough test

Oil breakthrough experiments were carried out on 150 µm thick and 2 cm wide parenchyma sample as shown in Figure 1a in SHS at 120°C. The equilibrated parenchyma tissue was put in contact with 20 mg of oil stained with Sudan Red for 2 h in similar conditions. The exposed surface area of 1 cm^2 was controlled using a removable microarray frame (Gene frame 25 µL system, Thermo Fisher Scientific, USA). Capillary forces and weight were the only possible driving forces. After contact, oil spills were scanned at room temperature in transparency mode (Scanner, model Perfection 4490 Photo, Epson, Japan) with a resolution of 3.1 µm/pixel. Only the red channel was acquired.

Large and medium-sized spills associated to coalesced droplets were preferably analyzed using radial distribution functions $g(r)$ as exemplified in Figures 1c–d for hexagonal periodic spills matching the shape of cells. Well-formed droplets with circular contours were interpreted instead after image segmentation as spherical caps with volume given by

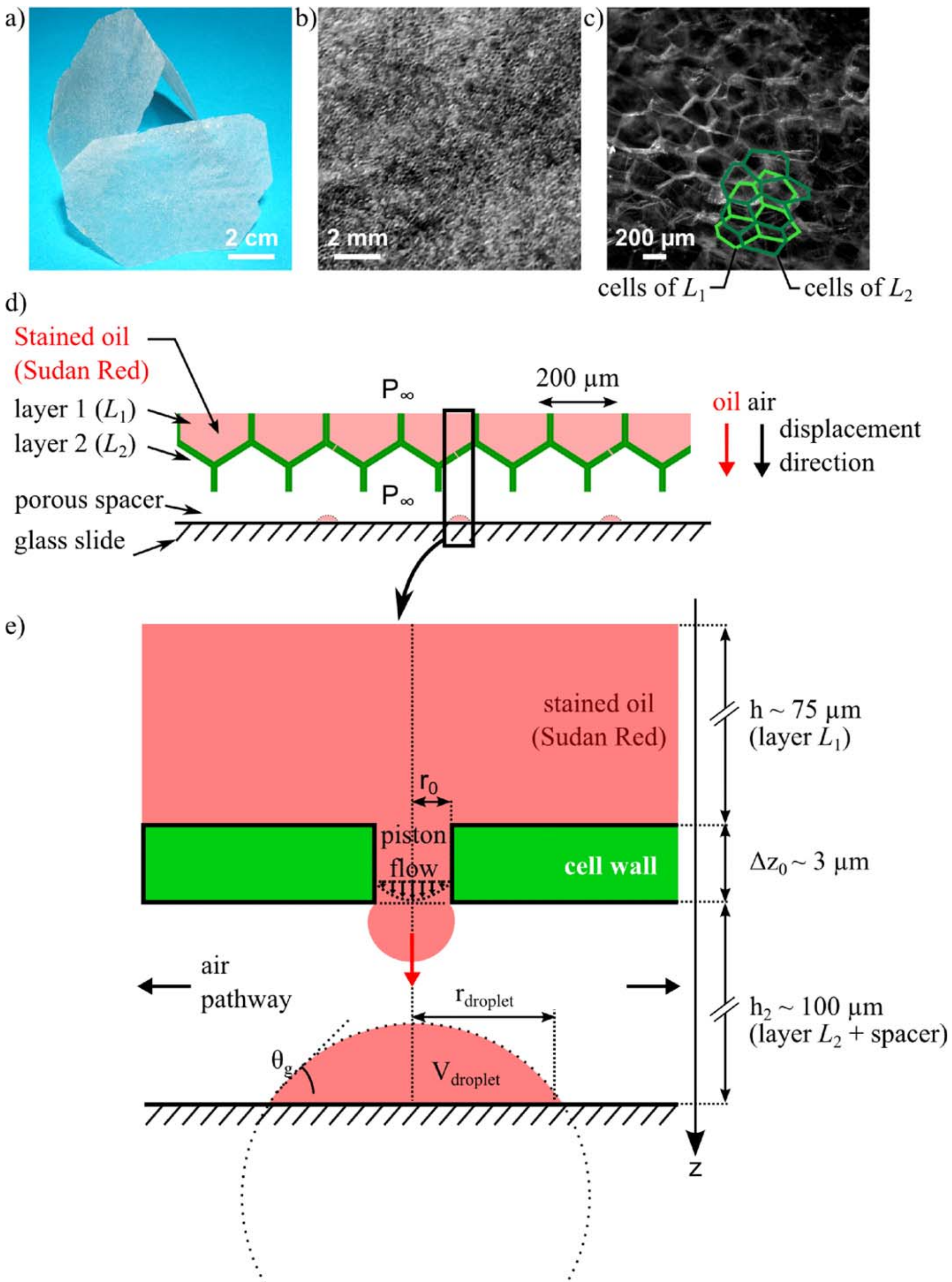

Figure 2. Principles of the method of reconstruction of defect sizes between layers L_1 and L_2 from breakthrough experiments presented in Figure 1.

Examples of microtomed potato tissues equilibrated in superheated steam and used for tests: (a) overview by transparency, (b) details in light reflection, and (c) cellular details in deep-UV epifluorescence (excitation 280 nm, emission above 310 nm). (d) Interpretation of oil-air cocurrent displacement at cellular scale in breakthrough experiments (gas pressures are equal on both sides of the tissue) and (e) relationship between the size of defects and the volume of accumulated droplets [see Eq. 16]. [Color figure can be viewed in the online issue, which is available at wileyonlinelibrary.com.]

$$V_{\text{droplet}}^{(T=25^\circ C)}=\frac{\pi\left(2-3\cos\theta_g+\cos^3\theta_g\right)}{3\sin^3\theta_g}r_{\text{droplet}}^3 \tag{15}$$

where r_{droplet} the radius of the droplet. The oil-glass contact angle θ_g was fitted from Eq. 15 and by measuring the weight of single droplets on a glass slide. A value of 23° ± 3° was found, close to the one of 28° reported in.[60] These relatively low values are explained by the preferential wetting of the glass by free fatty acids with tension-active properties. Based on the assumption of Poiseuille flow, Eq. 15 enabled also to

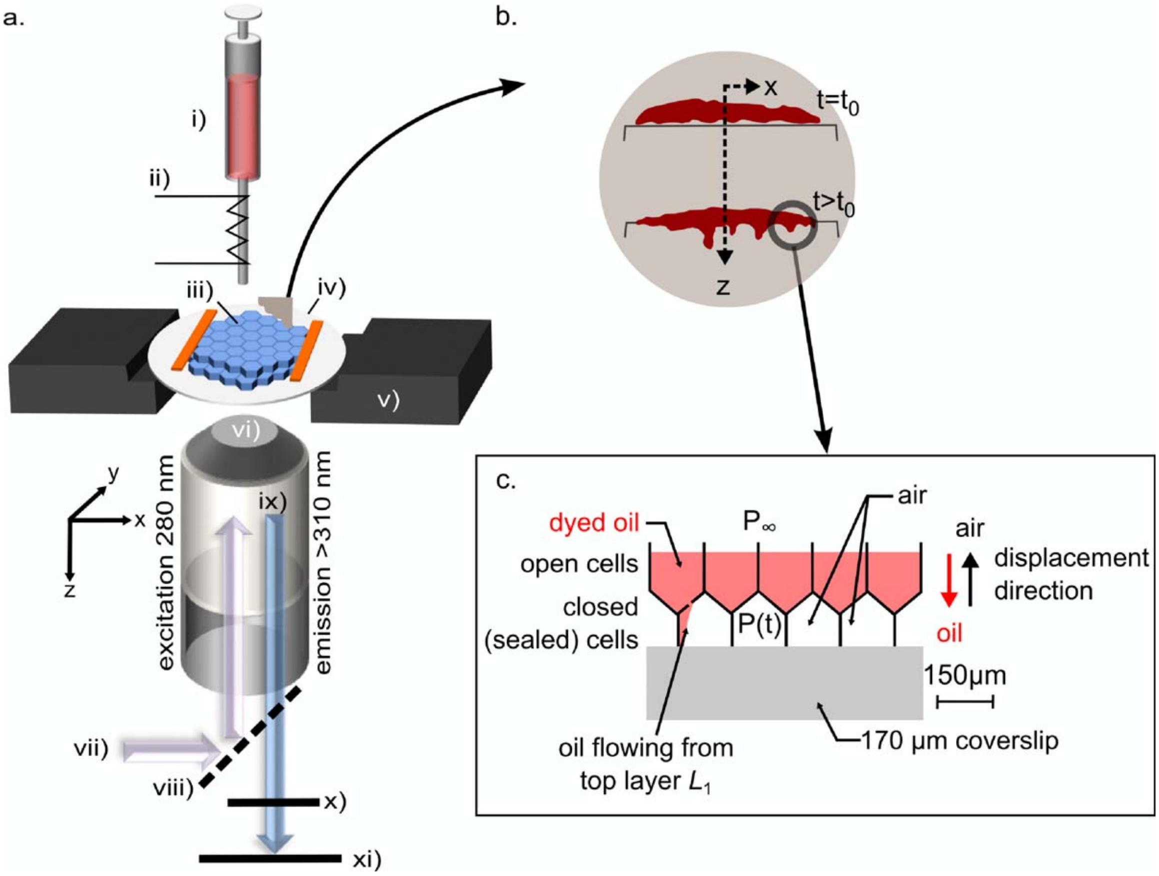

Figure 3. Experimental setup for dynamic observation of oil uptake at microscopic scale in epifluorescence using a deep-UV excitation: (a) overview, (b) contact time at t_0 and $t>t_0$, and (c) oil-air counter-current flow configuration.

(1) 20 μL microsyringe filled with dyed oil (in red, 1,6-diphenyl-1,3,5-hexatriene) at 120°C, (2) electrical resistance wrapped around the needle and thermocontrolled at 120°C, (3) potato tissue, (4) 0.17 mm thick quartz coverslip, (5) Peltier heated at 100°C, (6) objective lens in quartz, (7) UV synchrotron excitation beam, (8) dichroic mirror at 300 nm, (9) emission beam, (10) emission filter at 310 nm, and (11) electron multiplying CCD camera. [Color figure can be viewed in the online issue, which is available at wileyonlinelibrary.com.]

reconstruct the likely distribution of the defects matching the distribution of droplet sizes. The reconstructions rely on cylindrical defects with a length commensurable to the thickness of cell walls Δz_0 as shown in Figure 2. For each droplet, the radius r_0 of the equivalent cylindrical defect was given by

$$V_{\text{droplet}}^{(T=25°C)}=\frac{\rho_{\text{oil}}^{(120°C)}}{\rho_{\text{oil}}^{(25°C)}}\frac{\pi {r_0}^4}{8\mu_{\text{oil}}^{(120°C)}}\left(\rho_{\text{oil}}^{(120°C)}g+\frac{2}{r_0}\frac{\gamma^{(120°C)}\cos\theta_C^{(120°C)}}{h+\Delta z_0}\right)(t-t_0) \tag{16}$$

where $\rho_{\text{oil}}^{(T)}$ and $\mu_{\text{oil}}^{(T)}$ are the density and viscosity of oil at temperature T. At $T=120°C$, the values of 865 kg m^{-3} and 0.06 Pa s were chosen in agreement with.[61] Oil-steam surface tension $\gamma^{(T)}$ was assumed equal to the value obtained in air at the same temperature, that is 0.03 N m^{-1} from the same reference at 120°C. t_0 is the required time to fill the defect according to the law of Lucas-Washburn equation. Because it was much lower than 1 s, it was neglected in front of contact times with oil, t, of 2 h. Consistently with our experiments and because the excess of oil was removed, the oil height, h, was chosen equal to the thickness of the first cell layer (75 μm).

Dynamic imaging of oil uptake at microscopic scale

Oil percolation at cellular scale was monitored in time and space using a modified version of the methodology applied by Achir et al.[21] A bright deep-UV synchrotron source (DISCO beamline, Synchrotron Soleil, Gif-sur-Yvette, France) centered on 295 nm was replacing a 351/364-nm argon laser enabling the increase of autofluorescence yields while decreasing acquisition time down to 1 s. This setup was used to image simultaneously oil (emission in the range 400–500 nm) and cell walls (emission in the range 300–500 nm) in epifluorescence mode. Fluorescence emission above 300 nm was separated from emission with the help of a dichroic mirror (DM300, Zeiss, Germany) and collected at a frame rate of 1 Hz with a UV-VIS electron-multiplied charge-coupled device camera (Electron Multiplying Charge-Coupled Device, Digital Camera, model PIXIS 1024, Princeton). 16 bits intensity images (1024 × 1024 pixels^2) reached a resolution of about 1.2 μm pixel^{-1}.

Each sample was held on a quartz coverslip and was observed through oil immersion objective as represented in Figure 3. Dyed oil was preheated at 120°C and was transferred by means of a 20 μL microsyringe (Hamilton Co, Nevada). Oil was maintained at 120°C using a thermocontrolled film resistance folded around the needle. The sample

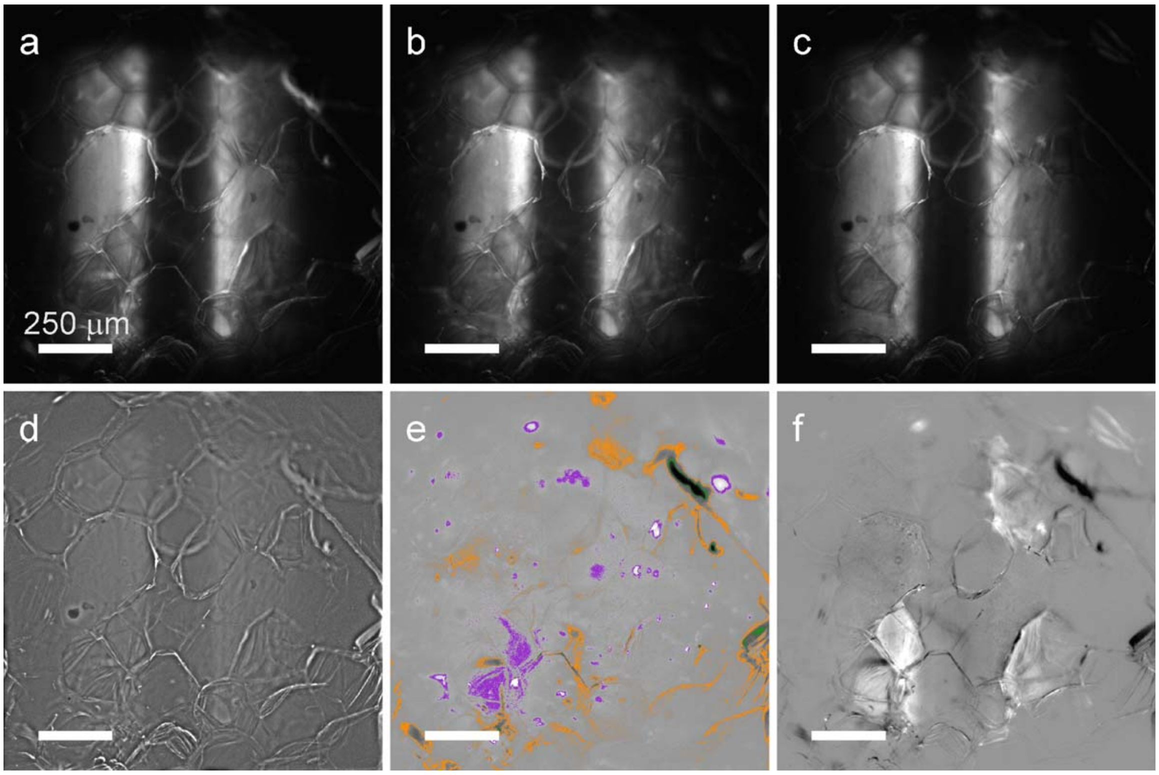

Figure 4. Typical intensity raw a–c) and background corrected d–f) images (downsampled to 256 gray levels).

Images a) and d) were acquired immediately after oil contact at t_0. Images b) and e) were acquired at t_0+1 s. Images c) and f) were acquired at t_0+75 s. Regions of image e) with intensity ranges 74 ± 10, 139 ± 10, and 189 ± 10 are plotted with green, orange, and violet contours, respectively. [Color figure can be viewed in the online issue, which is available at wileyonlinelibrary.com.]

was kept at an immediately lower temperature (100°C) on a heating microscope stage (Peltier PE 100-NIF, Linkam Scientific Instruments, UK). As shown in Figure 3 (inset ix), the sample comprised two cell layers denoted L_1 and L_2 for a total thickness larger than 200 µm (250 µm on average). Oil accumulation in L_2 was enabled by cutting L_1 above its sagittal plane while cutting L_2 near its junction with the third layer. The quality of the cut of each sample was checked under binoculars by transparence and by means of a thickness gauge. Once cells were washed and starch removed, they were dried in SHS at 120°C mounted on a 0.17 mm thick quartz coverslip to close the cells of L_2. Microscopic observations showed that adhesion was enhanced by residual tissues from the bottom of L_2 so that the use of glue was unnecessary. In particular, preliminary tests with epoxide glue caused more artifacts (obstructions) than much better sealing. The experiment was repeated 100 times with 75 results directly exploitable.

Image analysis

The beam flux with X-ray components removed was maximized by defocusing the beam at the outlet of the monochromator. The resulting structured lighting (two vertical bands) was removed systematically via homomorphic filtering.[62] As illustrated in Figure 4, it was applied between the reference image, denoted **R**, used as illumination pattern and the target image, denoted **I**. The calculations were performed in Fourier space as

$$\mathbf{I}_{\text{filtered}}=\exp\left(\text{FFT}_2{}^{-1}\left(\mathbf{W}\left(\text{FFT}_2(\ln(\mathbf{I}+1))-\text{FFT}_2(\ln(\mathbf{R}+1))\right)\right)\right)-1 \tag{17}$$

where **W** is the spectral response of a high-pass band Butterworth filter. Direct 2-D and inverse Fast-Fourier transforms are noted FFT_2 and $\text{FFT}_2{}^{-1}$, respectively. Only the real part of back-transformed result was kept. Examples of original and filtered images are depicted in Figures 4b,c and in Figures 4e,f respectively. Figure 4a is used as reference for both cases.

Oil uptake contribution was obtained by image subtraction involving a nonparametric method initially proposed by Bromiley et al.[63] for detecting tumors and modified by us for our purpose. The method is illustrated in Figure 5 using images 4e (source image denoted A) and 4f (destination image denoted B) as examples. It uses a binary scattergram (Figure 5a) to assess how a local intensity in A is transformed in destination image B, while assuming that the sample was not moved between both acquisitions. As a result, any initial Dirac distribution centered on intensity I_A in A appears as a continuous distribution in B. The three vertical lines in Figure 5a correspond to the intensity values 74, 139, and 189 in B of regions depicted in Figure 4e. Horizontal arrows in Figure 5b denote the intensity shift of the first mode between images A and B. Filled areas under each curve assessed consequently the amount of dyed oil in the considered region. Each distribution plotted vertically for all possible I_A values defines the so-called scattergram. Tangential filtering (anisotropic filtering keeping gradients and edges) applied to the scattergram enforced the regularity of the distributions with I_A. Distribution of I_B values corresponding to the three regions in **A** are plotted as three vertical lines in Figure 5a and as continuous distributions (on 256 gray level scale) in Figure 5b. The shift to the left-hand side of the first mode between A and B is associated to fluorescence bleaching whereas the apparition of a second mode is related to the apparition of a second population of dye (oil

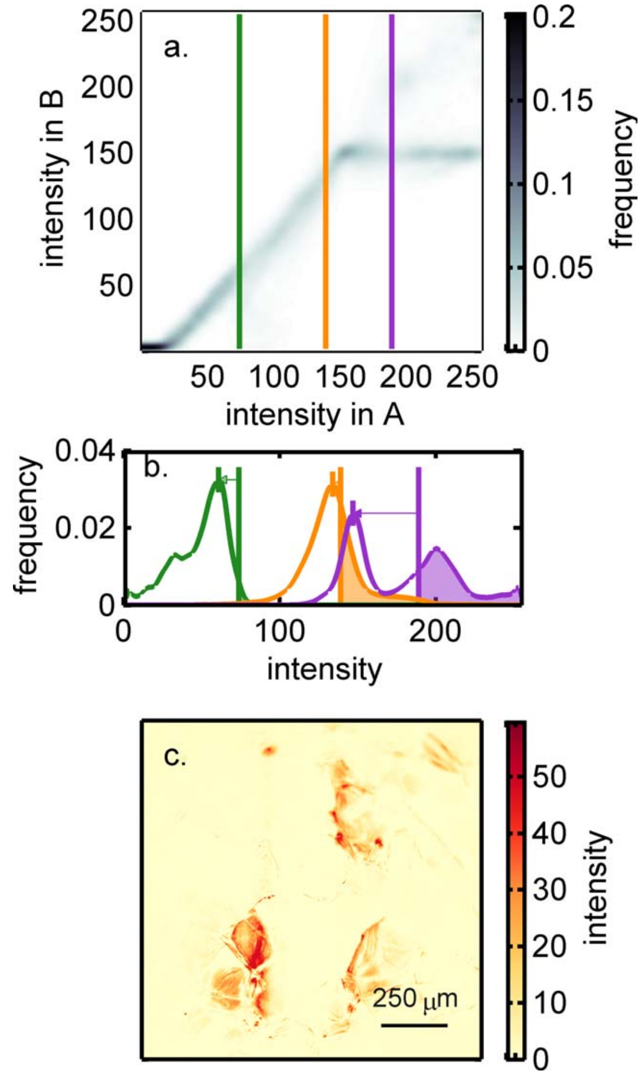

Figure 5. Principles of image subtraction between frames A (depicted in Figure 4e) and B (depicted in Figure 4f).

(a) 2-D-scattergram $S(x=IA,y)$ plotting vertically the distribution in intensity of pixels in B with the intensity IA in A. (b) Comparison of the intensity distributions of pixels in A (Dirac) and in B with initial intensities 74, 139, and 189 (see Figure 4e). (c) Result of the subtraction of frames A and B as calculated via Eq. 18. [Color figure can be viewed in the online issue, which is available at wileyonlinelibrary.com.]

percolation). Oil-related intensity was calculated therefore according to

$$(I_\mathrm{B}-I_\mathrm{A})_{\text{region of intensity } I_\mathrm{A} \text{ in } \mathbf{A}} = \int_{\max(I_\mathrm{A},\mathrm{mode}(I_\mathrm{B}))}^{+\infty} f(I)\,dI \qquad (18)$$

The image difference corresponding to Figures 4e,f is shown in Figure 5c as an intensity image. It is worth noticing that the method is said nonparametric as it uses the real distribution of intensity images to determine the likelihood of an "excess" of fluorescence associated to the presence of dyed oil. Besides, the method is particularly efficient to correct nonlinear fading, in particular when bleaching rate between A and B depends on the intensity in A (first-order bleaching decay). When oil percolation invaded the whole field, Eq. 18 could not be applied (regions filled with oil cannot be separated from native regions), and expansion series of Eq. 17 was used instead, and frame subtraction was calculated as a relative intensity variation, denoted $\Delta_{a,b}\mathbf{I}$

$$\mathrm{FFT}_2\left(\log\left(\Delta_{a,b}\mathbf{I}+1\right)\right)=\sum_{n=a}^{n=b-1} \mathbf{W}\left(\mathrm{FFT}_2\left(\log\left(\mathbf{I}_{n+1}+1\right)\right)-\mathrm{FFT}_2\left(\log\left(\mathbf{I}_n+1\right)\right)\right) \qquad (19)$$

Equation 19 assumes that frames A and B are separated by $b-a>0$ frames so that high-frequency components can be cumulated between frames with good signal-to-noise ratio. A proprietary code was developed on Matlab (Mathworks, Massachusetts) to perform the calculations on a cluster. More than 2.5×10^4 images were processed.

Oil saturation at the scale of single cells

Cell contours of top and bottom layers were digitalized in (x,y) plane by coinciding the vertices of hexagons with cell junctions. For each pixel in the area of one cell, the measured intensity, I_oil, resulted from fluorescence and light scattering along the vertical axis z. Due to the overlap between cells of the first and second cell layers, the volume observed in plane (x,y) corresponded to the limit of a cell of the top layer and included also parts of cells from the bottom layer. Information from the first and second layer was separated by noticing that the measured intensities presented two stable and separable maxima: once the cells of the first and the second cell layer were respectively filled with oil. By normalizing the measured intensities with the first maximum, an estimate of the cell saturation was achieved: 0 for an empty cell, 1 for a filled cell of the top layer (L_1), larger than 1 when cells of the bottom layer (L_2) are also filled with oil. The reconstruction of the cell arrangement and filling kinetics along the z direction relies on the separation of time-scales associated to the filling kinetics of cells of L_1 and L_2. Additional details can be found in the companion paper.[16]

By considering that one cell from an arbitrary layer A (i.e., L_1 or L_2) in contact with M cells (usually $M=3$) of the next layer B, the effective cell saturation as experimentally assessed, $S_\mathrm{o,measured}$, was interpreted as a linear combination of saturation of cells from layers A and B

$$\begin{aligned} S^{(t)}_\mathrm{o,measured} &= \frac{1}{V_\mathrm{cell}}\int \delta(x,y,z,t)\,dxdydz = S^{(t)}_\mathrm{o,A}+\sum_{i=1}^{M} s_i S^{(t)}_{\mathrm{o,B},i} \\ &\approx \frac{1}{\mathrm{I}_\mathrm{max}}\int \mathrm{I}_\mathrm{oil}(x,y,t)\,dxdy+\sum_{i=1}^{M} s_i S^{(t)}_{\mathrm{o,B},i} \end{aligned} \qquad (20)$$

where $S_\mathrm{o,A}$ is the saturation of the considered cell in layer A; $S_{\mathrm{o,B},i}$ and s_i are the saturation and the surface area fractions of cells $i=1$. M in layer B overlapping the cell considered in A. The delta function δ(x,y,z,t) is equal to 1 at time t when oil is present and 0 otherwise.

Equation 20 applied to all observed cells led to a large system of linear equations where the unknowns were $\left\{S^{(t)}_{\mathrm{o},L_1,i}\right\}_{i=1..N_1}$ and $\left\{S^{(t)}_{\mathrm{o},L_2,j}\right\}_{j=1..N_2}$, with N_1 and N_2 the number of observed/interpreted cells. The system was dramatically simplified by noticing the events related to the filling of cells of L_1 and L_2 were separable in time. The normalized intensity I_max was assigned to the maximum value reached when

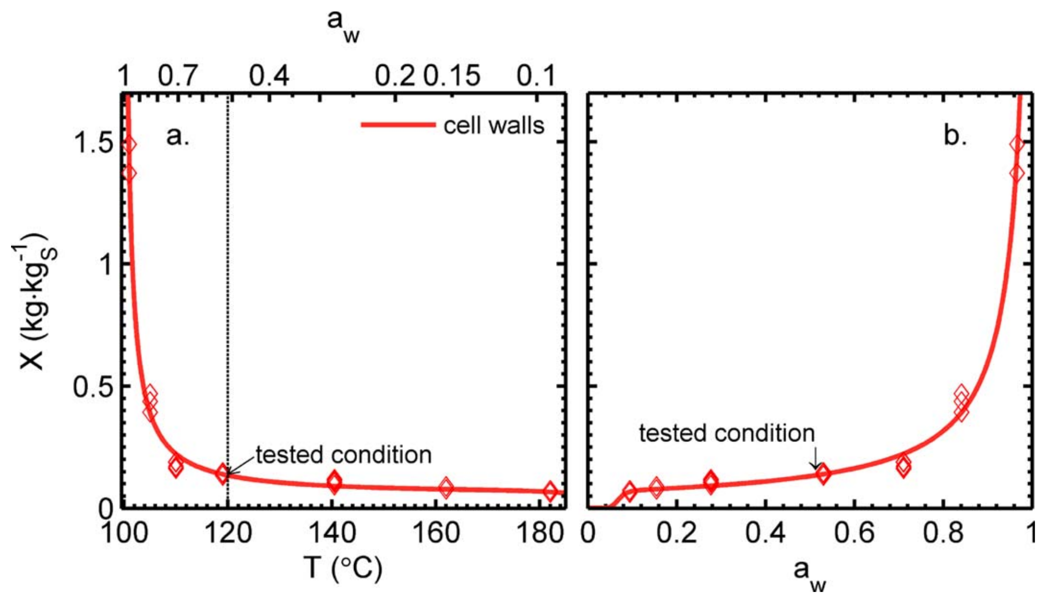

Figure 6. Isobaric water desorption curves of parenchyma cell walls.

Residual water content (*X*, solid basis) is plotted versus (a) equilibrium temperature (*T*) and (b) water activity (a_w). The condition used to study oil penetration is indicated as "tested condition." [Color figure can be viewed in the online issue, which is available at wileyonlinelibrary.com.]

the considered cell of L_1 was fully filled. Hence, the complete filling of a cell of L_2 corresponds to a local saturation set to a value of two (two cells). Filling times t_{sat} were estimated as times necessary to obtain saturation equal to 1 (or 2 for cells of L_2), starting from t_0, the instant before oil is added on products

$$\begin{aligned} t_{sat,L_1} &= t_{(I=I_{max},L_1)} - t_0 = t_{(S_o=1)} - t_0 \\ t_{sat,L_2} &= t_{(I=I_{max},L_2)} - t_0 = t_{(S_o=2)} - t_0 \end{aligned} \tag{21}$$

Lag time t_{lag} was defined as the delay between the filling kinetics of the connected cells of L_1 and L_2. It is calculated from the difference at the time to reach saturation of 0.5 and 1.5, respectively

$$t_{lag} = t_{(S_o=1.5)} - t_{(S_o=0.5)} \tag{22}$$

Results and Discussion

Isobaric sorption properties of water in parenchyma cell walls

Water sorption properties in isobaric conditions, at 100 kPa, are plotted in Figure 6 as residual water content relative to solid content, X, versus temperature, T, and equivalently, versus water activity calculated according to Eq. 2. Each single sorption curve can be considered as a collection of sorption isotherms at different temperatures in isobaric conditions. Collected isotherms of cell walls were successfully fitted with the GAB Eq. 7 using a Nelder-and-Mead simplex search method. Corresponding fitted parameters are listed in Table 1 and compared with the values for artificial cell walls[65] (comprising cellulose, pectin and xyloglucan). Uncertainties on fitted parameters were evaluated by means of a bootstrap sampling procedure involving 2000 samples. In the GAB model, the parameter X_m measures the availability of active sites for water sorption. The values of $C_g(T)$ and *K(T)* (see Eq. 7) complete the description by assessing the nature of interactions between solid matrix and adsorbed water. Values of $C_g(T)$ (see Eq. 7) are tabulated at 120°C and at room temperature in Table 1 to enable comparison with literature values. All conditions showed $C_g(T) \gg 1$ along with $K(T) \approx 1$. The common interpretation of these values is that the desorption isotherms depend on two desorption energy levels: one for the monolayer and one for the multilayer, which was found close to the latent heat of vaporization of bulk liquid water. According to Khalfaoui et al.,[66] corresponding isotherms tend to be sigmoidal so as the isobar depicted in Figure 6. Significant net isosteric heat of desorption appeared noticeable only at very high temperatures above 170°C ($a_w < 0.15$). Similar conclusions were met using the Clausius–Clapeyron relation instead of the GAB model.

In real French fry products, surface cells lose their content after cutting whereas cells beneath remain filled with starch molten during frying. By contrast, sorption properties of potato starch[67,68] differ from those of cell walls with $C_g(T) \approx 1$ along with $K(T) \approx 1$, corresponding to no significant energy barrier between sorption layers and bulk.

The state at 120°C and a_w of 0.51 in equilibrium with pure steam was chosen as reference for the experiments (see Figure 7a at 120°C with Eqs. 2 and 3 for the equivalence between T and a_w). This state is consistent with conditions found in the crust of French fries as detailed in.[27] Similar conditions have been described by Thussu and Datta[30] after 24 and 54 s of frying a potato strip of thickness 5 mm at 140°C and 170°C, respectively. Samples were stored before experiments at the same relative humidity ($a_w = 0.51$).

Mimicking postfrying conditions in oil percolation experiments

During oil percolation experiments, the product was kept at 100°C ± 1°C and oil was introduced at a temperature ranging between 115 and 120°C. These conditions were close to real postfrying conditions, where the crust continues to be heated during few seconds by surface oil before rapidly cooling down. The main discrepancy between our

Table 1. GAB Parameters (see Eq. 7) for Potato Cell Walls Inferred from Isobaric Data Plotted in Figures 6 and 7a

	Values for Potato Parenchyma Cell Walls (This Work)				Values for Artificial Parenchyma Cell Walls from Fanta et al.[64] (± 95% Confidence Intervals)
		Percentiles from Bootstrap Sampling (2000 Samples)			
Parameter (units)	Likeliest Value	5th	50th	95th	
C_{g0}(-)	4.4×10^{-25}	3.6×10^{-32}	2.2×10^{-15}	3.9×10^{-7}	–
ΔH_C (kJ mol^{-1})	2.3×10^{2}	73	1.4×10^{2}	3.1×10^{2}	–
K_0(-)	0.99	0.80	0.87	0.93	–
ΔH_K (kJ mol^{-1})	1.34×10^{-5}	2.7×10^{-6}	9.1×10^{-6}	3.5×10^{-5}	–
X_m(-)	6.7×10^{-2}	7.3×10^{-2}	7.7×10^{-2}	8.2×10^{-2}	0.15 ± 0.005
C_g (at $T = 25°$C)	∞	–	–	–	∞
K (at $T = 25°$C)	$0.99 \approx 1$	0.80	0.87	0.93	$1.0 \pm 2{\cdot}10^{-4}$
C_g (at $T = 120°$C)	∞	–	–	–	–
K (at $T = 120°$C)	$0.99 \approx 1$	0.80	0.87	0.93	–

experiments and "real-life" frying is that the product and oil could not reach temperatures significantly lower than 100°C in our experiments. In details, additional subtle differences might have also been introduced such as a possible short cycle of water sorption-desorption during handling and subsequent heating step. Instead of introducing any artifact, these conditions were known to prevent any condensation of steam at the surface of cell walls, which could have changed in turn their wetting properties. Finally, our experimental setup granted that capillary pressure and gravity were the only driving forces enabling oil to percolate through the product tissue. As the potato tissue was kept almost isotherm, the magnitudes of capillary and viscous forces were assumed also constant. To reach a comparison with "real-life" postfrying conditions, Figure 7b plots the theoretical gas pressure during cooling according to the composition of the partial pressure of water vapor. The values were calculated according to Eqs. 6 and 7 by considering that the residual steam was not escaping the product during cooling. As a result, the presented pressure drops represent upper bounds of real values. The equilibrium curves demonstrate that pressure drop can occur far above T_{sat} during postfrying. Predicted negative pressure gauges are in the range of values reported experimentally[13,14,36] for air fraction about 10–20%.

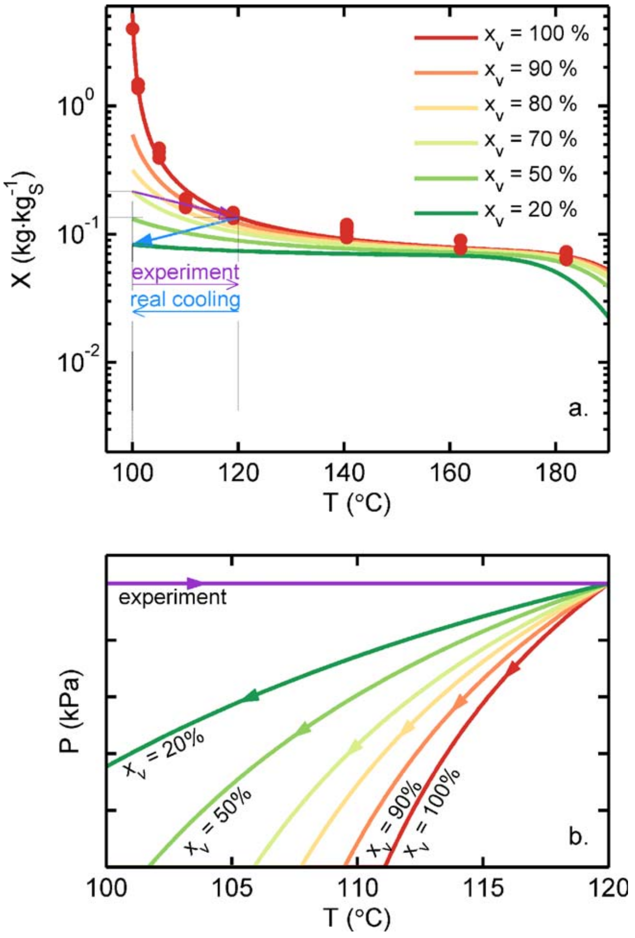

Figure 7. Thermodynamical equilibrium curves of cell walls in frying ($x_v = 1$, increasing T) and cooling ($x_v < 1$, decreasing T) conditions according to the volume fraction of water vapor (x_v).

(a) Residual water content (X, solid basis) vs. T at thermal equilibrium; (b) Equivalent total gas pressure (P). Continuous curves of X and P were inferred from Eqs. (6) and (7) using isobaric curves depicted in Figure 6 (assumptions are detailed in Properties of Steam in the Crust During Frying and Postfrying Section). [Color figure can be viewed in the online issue, which is available at wileyonlinelibrary.com.]

Cell connectivity ratio enabling oil to pass from one cell layer to next one

Achir et al.[21] showed that oil percolation in undamaged fried potato tissues is inhomogeneously distributed due to the low permeability of connected cells. Oil was assumed to flow mainly through intercellular spaces at cell junctions (see Chapter 3 of[69]) with radii ranging about few to tens micrometers or through sparingly distributed channels connecting cells, so-called plasmodesmata[60] and with diameters about 100 nanometers. Both possible passages were investigated using a breakthrough test (see Figure 1) lasting 2 h at 120°C, much longer than frying and cooling stages. The results corresponding five independent repetitions plotted in Figure 8. Oil was put in excess so that it is reasonable to assume that the size and number of leaks were only determined by the size and number of defects.

Droplets covered only from 2.6 to 13.5% of the whole surface confirming the extremely low connectivity of undamaged parenchyma cells reported by Achir et al.[21] The five depicted samples covering 5 cm^2 acquired with a spatial resolution of 323 pixels mm^{-1} exhibited 579 coalesced spills and 757 droplets with circular contours for a total of 1336 isolated spills. The morphology and spatial distribution of large spots were analyzed by plotting their radial distributions at two typical scales: ranges 0.2–10 mm and 0.025–2 mm, in Figures 8 and 9a, respectively. Droplets matching the spherical cap model (see Figure 2) were specifically

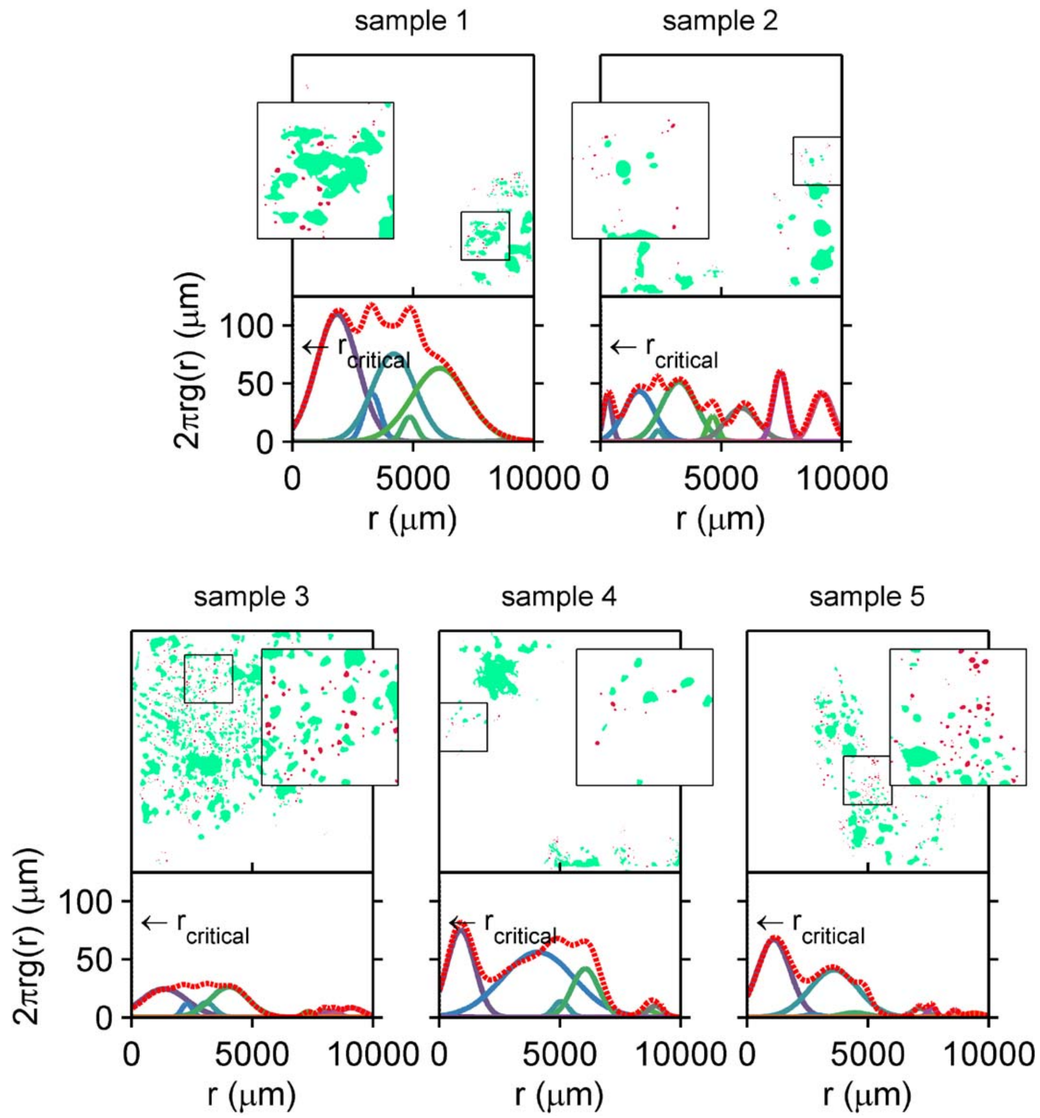

Figure 8. Oil spills corresponding to five different samples.

Results are depicted as images in false color images (1 × 1 cm^2) and as radial distributions (see their interpretation in Figure 1). Spills appearing as coalesced droplets are depicted in green and well-formed ones obeying to the scenario depicted in Figure 2 are presented in red. Each inset represents region details magnified five times. Radial distributions corresponding to each test are plotted beneath with main peaks deconvolved as a sum of Gaussians. [Color figure can be viewed in the online issue, which is available at wileyonlinelibrary.com.]

analyzed individually in Figure 9b to determine the distribution of defects which could explain them.

Main statistics of spots sizes and distances are summarized in Table 2. At large scale, the average spot size and the likely distance between defects were given by the first peak and the distance to next one, respectively. Spills were on average separated by 0.22 ± 0.05 mm. The distribution of coalesced droplets presented two typical modes: 1.39 ± 0.59 and 0.30 ± 0.23 mm. Half of spills had circular shapes and could be reasonably approximated as spherical caps with radii ranging from 3.5 μm up to 46 μm and volumes ranging from 12 μm^3 to 27 × 10^3 μm^3 according to Eq. 15. For comparison, a spill volume commensurable to the volume of a L_1 cell, that is 2.4 × 10^6 μm^3, would require a defect radius of about 0.42 μm for a spill radius of 205 μm. This large spill radius value confirmed that droplets with circular shape were likely to correspond to one single defect in one of the three cells of L_1 in contact with the cell of L_2. Equation 16 gave cylindrical defects with radii ranging from 7.8 to 100 nm with a median value of 40 nm. Their small sizes were consistent with an assumption of oil flow through plasmodesmata. According to Robards,[70] their numbers in cells vary between 10^3 and 10^5. The junctions connect adjacent cells and enable mass transfer of molecules in living cells. Little is nevertheless known on their structure once there are subjected to SHS.

Filling kinetics of cells by oil

Typical Results and Reconstructions. Microscopic experiments were carried out in conditions close to those used to identify the breakthroughs between L_1 and L_2. As the goal was to sample the filling kinetics of cells within each layer, the cutting procedure was updated to reach thicker sections ranged between 150–300 μm. In connection with macroscopic permeability experiments, the time window was set from 4 up to 25 min with a frame rate of 1 Hz. Each

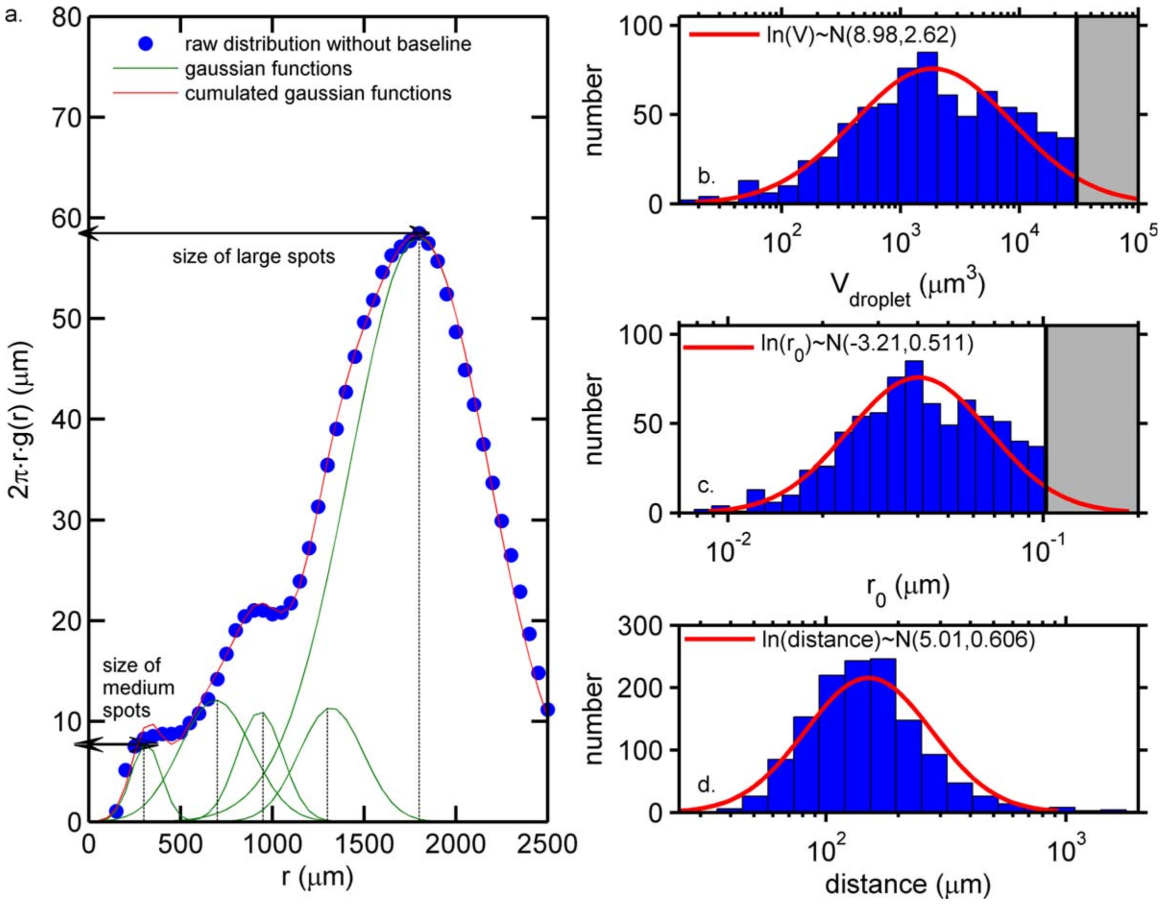

Figure 9. Finest details corresponding to Figure 8.

(a) Deconvoluted radial distribution of sample 1 and (b) Distribution of volumes of well-formed droplets associated to samples 1–5. (c) Corresponding distribution of defects from Eqs. (15) and (16) (see Figure 2) and (d) minimal distance between defects. [Color figure can be viewed in the online issue, which is available at wileyonlinelibrary.com.]

series comprised from 400 to 3000 frames. To account for the low damage ratios, 75 series independent were collected in similar conditions.

Figure 10a presents typical observations and interpretation of percolation experiments carried out at a magnification of ×10 (see Figure 3). The initial small synchrotron beam generated at the output of the binding magnet was defocused to illuminate fully the observed region with a wider collimated square 3 × 3 mm^2 beam. The optical process created a structured lighting, acquired in raw images, which was removed during post-treatment by means of homomorphic filtering (see Eq. 17) and Figure 4). In corrected images, residues of nonuniform lighting appeared as two rectangular lines in the images (see Figure 10a). They corresponded to high-frequency components, which were not properly removed by an estimation of the background from the low-frequency components of the image alone. Three particular events from a same typical series comprising 1500 frames are represented: the initial image at t_0 before contacting the potato tissue with oil; the intermediate image at t_1 very close to t_0, where all cells of L_1 are filled with oil; a final image after several minutes of contact with oil at t_2, where some cells of L_2 are seen filled with oil.

Once the signal of oil and cell were separated (see Eq. 19 and Figure 5), frames were assembled as composite red-green images (see Figure 10a). The green channel was

Table 2. Distribution of Oil Spills Presented in Figures 8 and 9: Large and Medium Spills Were Analyzed from Radial Distributions Whereas Smallest Ones Were Analyzed by Image Segmentation and Morphology Analysis

Class of spills	Average Radius (μm)	Distance (μm) To the first next spot	Distance (μm) To the second next spot	Defect radius (μm)
All spots (total 1336)	45±9	220±50	322±87	No model available
Large spots[a]	1390±590	2970±1270	3830±1340	
Medium spots[a]	300±230	600±430	1200±600	
Small spots matching the spherical cap model (total 757)[b]	20±3	274±80	408±122	$4.6 \times 10^{-2} \pm 2.2 \times 10^{-2}$

±: Confidence interval at 95%.

[a] From radial distribution.

[b] From image segmentation.

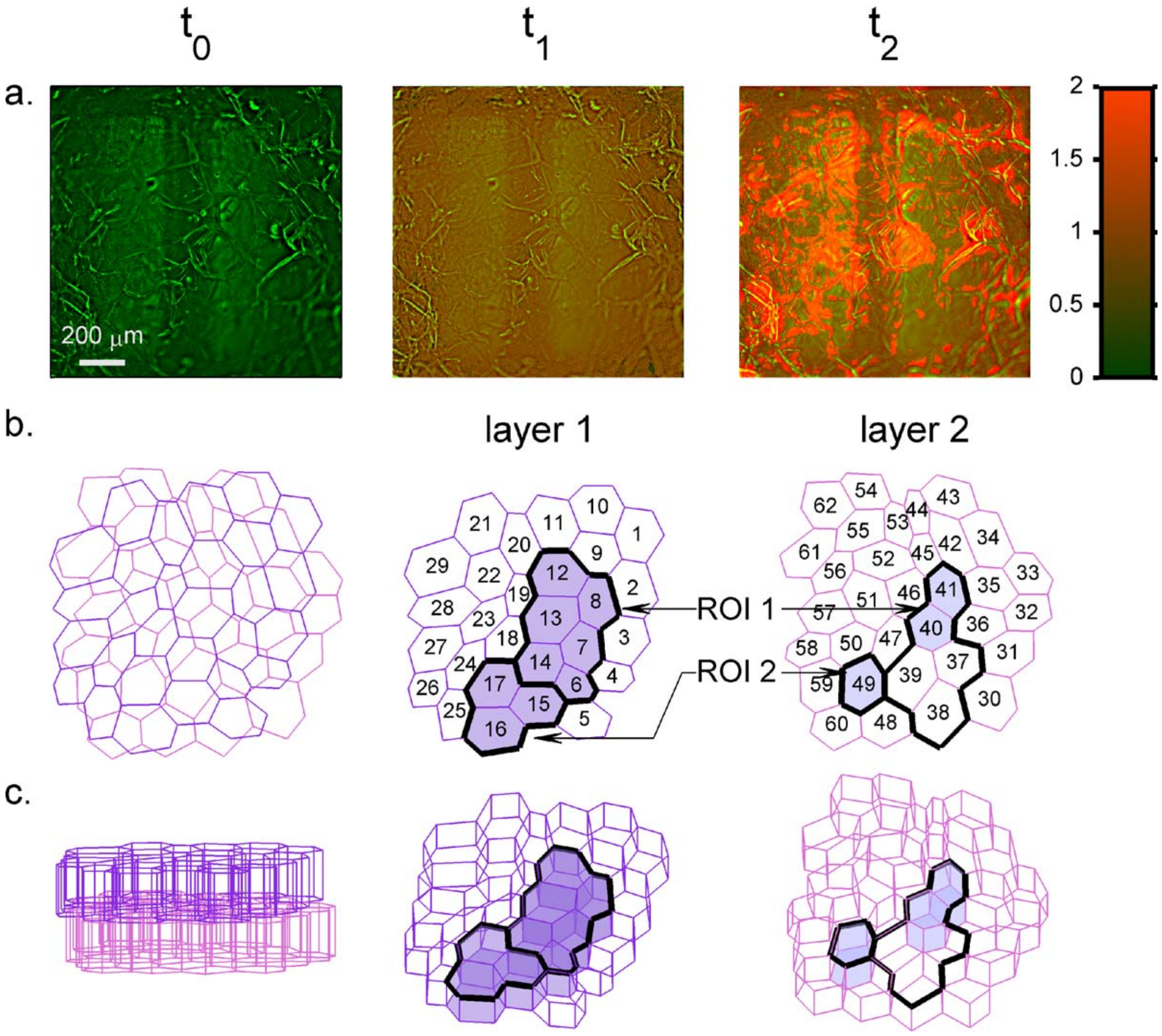

Figure 10. (a) Composite images with structured lighting removed (cell wall signal is associated to the green channel and oil to the red channel) before adding oil (t_0), once all cells of L_1 are filled with oil (t_1), after some cells of L_2 are filled with oil (t_2); (b) Cells tessellated in 2-D with irregular hexagons; and (c) Corresponding extruded hexagonal prisms.

Colored cells from ROI 1 and ROI 2 are filled or partly filled with oil at the end of acquisition. [Color figure can be viewed in the online issue, which is available at wileyonlinelibrary.com.]

assigned to cell walls and the red one to oil. The subtraction procedure uses the image t_0 as reference. It is emphasized that the very low read noise of the photoamplified CCD camera and the high depth (2^{16}) of the analogic-numeric conversion enabled us to acquire independently very low or high signals while keeping constant the gain during the whole experiment. A slow signal fading was however observed due to the photobleaching of phenolic constituents[71] after continuous exposure to deep UV and due to the ageing of the CCD gain register. Most of the signal loss was, however, recovered in a "natural way" by the subtraction procedure (see Eq. 18), which takes into account the drift of main fluorescence peak of each isointensity region.

Additional interpretation was gained by the tessellation of observed cells in two and three dimensions as presented in Figures 10b,c, respectively. Cell walls were identified from two independent procedures: *a posteriori* from a sequence of images in 2-D (when the cells are filled with oil or not) and *a priori* from vertical stacks of images accumulated automatically by displacing regularly the focal plane. The shape of real cells is a hexagonal prism capped with half a rhombic dodecahedron. Because the tetrahedral angles at the junction of two-cell layers could not be determined with enough accuracy, they were simplified as irregular hexagonal prisms with flat ends as discussed in pioneering microscopic works.[72–74] Cells of Figure 10b were continuously numbered from 1 to 29 in L_1 and from 30 to 62 in L_2. It is important to notice that each cell of L_1 is placed on top of three cells of L_2 as illustrated in Figure 10b in column t_0.

In the presented study, oil saturation of each cell layer was determined from the integration of the oil signal intensity over the 2-D cell contours from Eq. 20. Oil uptake in cells of the regions of interest, denoted ROI 1 and ROI 2, is analyzed specifically in Figures 11 and 12, respectively. ROI 1 comprises cells 6–8 and 12–14 in L_1 and cells 37–41 in L_2. ROI 2 includes cells 15–17 in L_1 and cell 49 in L_2 (as depicted in Figure 10b). The corresponding results as saturation kinetics are shown in Figures 11 and 12. As all cells of L_1 were cut and in direct contact with the oil droplet, they were filled with oil without almost any delay. The steady intensity value integrated over each cell of L_1 was chosen as reference to cumulate the intensity associated to the

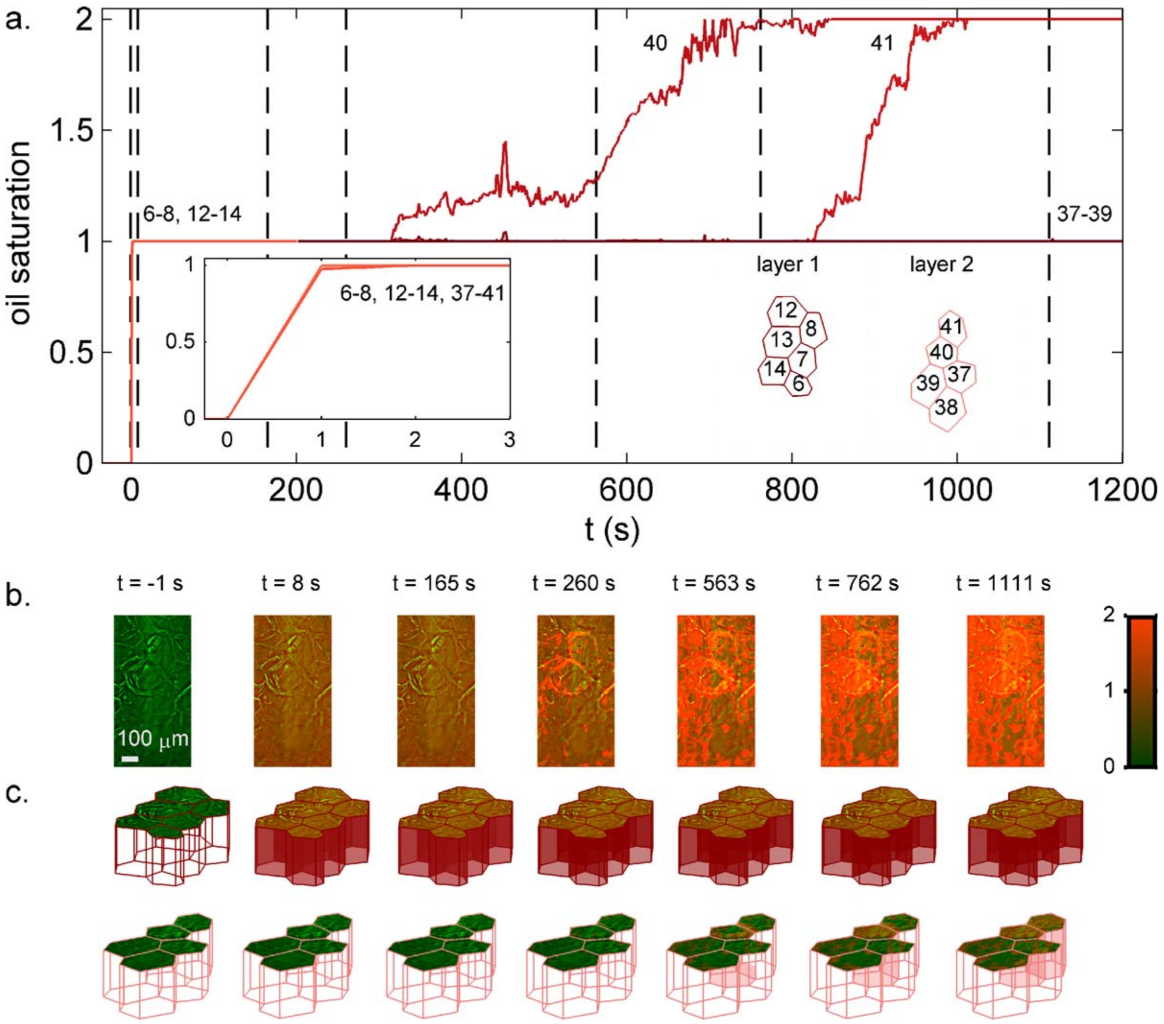

Figure 11. Dynamic of oil percolation of cells of ROI 1 in Figure 10.

(a) Oil saturation of individual cells of L_1 and L_2 (numbered 6–8, 12–14, and 37–41, respectively) corresponding to the sample depicted in Figure 10 and calculated according to Eqs. (19) and (20); (b) Composite image details and (c) 3-D reconstructions of L_1 and L_2. Oil level in each cell is displayed relatively to oil saturation. Oil saturation was expressed as the cumulating filling ratio of an equivalent vertical path connecting L_1 and L_2 (1 = full filling of the cell in L_1, 2 = full filling of the cell in L_2). [Color figure can be viewed in the online issue, which is available at wileyonlinelibrary.com.]

subsequent filling of the cells beneath. By contrast with cells of L_1, only few cells (ca. 10–30% in the observed areas) of L_2 were filled with oil with a filling ratio, also called saturation, which remained incomplete at the end of the experiment. The proposed interpretation of the sequence of images in space (i.e., along the vertical direction) was in full agreement with spills observed during breakthrough experiments. The low occurrence of cells of L_2 filled with oil matched the estimated probabilities of connection between two adjacent layers (see part 4.3). It was therefore confirmed that the same phenomena were observed in both cases.

To make the interest of such experiments more obvious: the tested conditions placed a large synchrotron (354 m of circumference) immediately below the crust of a hypothetical French fry and the penetration of oil was monitored with an observer positioned in the crumb. Although this description is extreme and slightly exaggerated, it shows our intent and the way the presented results can be analyzed to understand oil uptake in "real-life" conditions. In details, the dynamics of filling of L_1 were as fast as expected in real postfrying conditions (i.e., below 1 s without exceeding few seconds). Oil percolation from L_1 to L_2 occurred conversely on much longer time-scales (several minutes to hours in tested conditions) while remaining highly heterogeneous in space. Since the cells were emptied (no starch), the role of molten starch obstructing cells[75] could not be invoked to explain these heterogeneities as previously discussed by Achir et al.[21] Filling kinetics of the cells of L_2 exhibited a broad range of step shapes associated to time-scales varying between 165 and 1200 s, including: exponential shape, linear shape, two successive steps. In addition, a broad distribution of lag times separates the filling of connected cells of L_1 and L_2. When no filling of cells of L_2 was observed, it could be proven that the cells of L_2 were absolutely impervious to oil. Longer acquisition times would have been required to reach an absolute conclusion. However, long-term observations on large parenchyma tissues (see Figure 8 showing oil spots in L_2) demonstrated that only few cells (ca. 10%) of L_1 are connected to L_2.

First Interpretations. Oil uptake in cells of L_1 occurs on time-scales shorter than the acquisition time of the camera. Thus, the detailed mechanisms of oil percolation in L_1 were

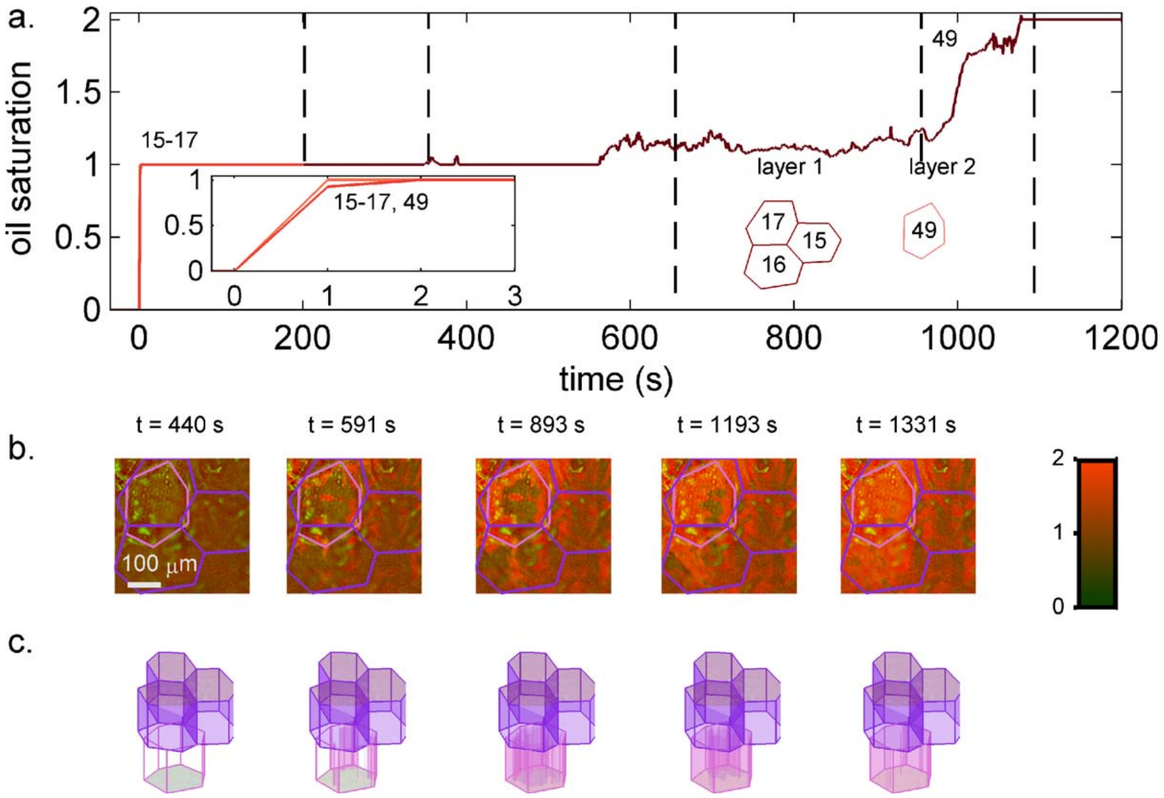

Figure 12. Dynamic of oil percolation of cells of ROI 2 in Figure 10.

(a) Kinetic of oil percolation between cells of L_1 and L_2 (numbered 15–17 and 49, respectively) corresponding to the sample depicted in Figure 10 and at different times (440, 591, 893, 1193, and 1131 s) after t_0. Images are in false colors (dark violet for L_1 filled by oil and light violet for oil percolating in L_2); (b) Composite image details; and (c) 3-D reconstructions of L_1 and L_2. [Color figure can be viewed in the online issue, which is available at wileyonlinelibrary.com.]

not identifiable. However, the slower oil uptake in cells of L_2 offered a sufficient time resolution to identify the main controlling phenomenon. In Figure 12, oil uptake is observed in L_2 once all L_1 cells are completely filled. According to intensities observed in composite images, oil propagated from cell walls to the center (and not the opposite). This suggests that oil adhered to cell walls regardless the original position of the defect, reached the bottom of L_2 and finally filled the cell.

The detailed routes followed by oil to percolate from L_1 to L_2 were difficult to identify from microscopic observations. It required a higher magnification and an intensive sampling of large surface areas to locate where meniscuses grew and infiltrated the second cell layer. Systematic observations carried out at a double magnification enabled to collect scarce infiltration events. One of them is reproduced in Figure 13. The observations confirmed the previous mechanism. Oil infiltrated along a cell wall of L_2. The flow was initiated from the common junctions between L_1 cells numbered 1–3. After a long lag time, the meniscus expanded fast while avoiding the center of the cell. The higher oil intensity at cell walls demonstrated the dominating role of capillary forces on oil penetration as discussed in Properties of Steam in the Crust During Frying and Postfrying Section. By contrast with oil, air as a nonwetting phase remained in the central region of the cell. The proposed description of oil-air biphasic flow is very similar to those proposed by Cortés et al.[15] on microchannels initially filled with steam. The absence of steam (condensable phase) does not seem to alter the conclusions when the results are extrapolated to real conditions.

Percolation lag times and filling times

Figures 10–13 show particular observations. Reliable interpretations were achieved by repeating the similar analyses for about 75 series of observations (more than 3×10^4 frames). Oil percolation kinetics were spread over several time scales. They were analyzed as lag times and filling times from Eqs. 21 and 22. Statistics derived from filling kinetics of 433 cells of L_1 and 46 cells of L_2 are presented in Figure 14. In details, filling kinetics of cells of L_1 and L_2 were almost self-similar with a filling time 100 times longer for L_2. Both kinetics were additionally asynchronous and separated by long lag times lasting from 10^2 to 10^3 s.

Proposed mechanisms of oil-air flows in potato crusts

Oil penetration in emptied parenchyma tissues was observed in simulated postfrying conditions as highly inhomogeneous in time and space. The dynamic behavior in presence of cellular structure is outstanding and does not fit with conventional descriptions of crude oil flow in disordered porous media such as rocks.[37,76,77] The presence of significant lag times is a major deviation to simplified descriptions proposed for capillaries with uniform section. The presence of cell walls between cell layers slows down dramatically the ability of oil to penetrate deeply inside potato products. This strong barrier effect was observed without any starch contribution (starch is not present in cells in our experiments). In addition, it must be noticed that air (incondensable phase not directly observable) was also present in cells. Biphasic liquid-air flows in porous media are well known to be affected by the topology of connected

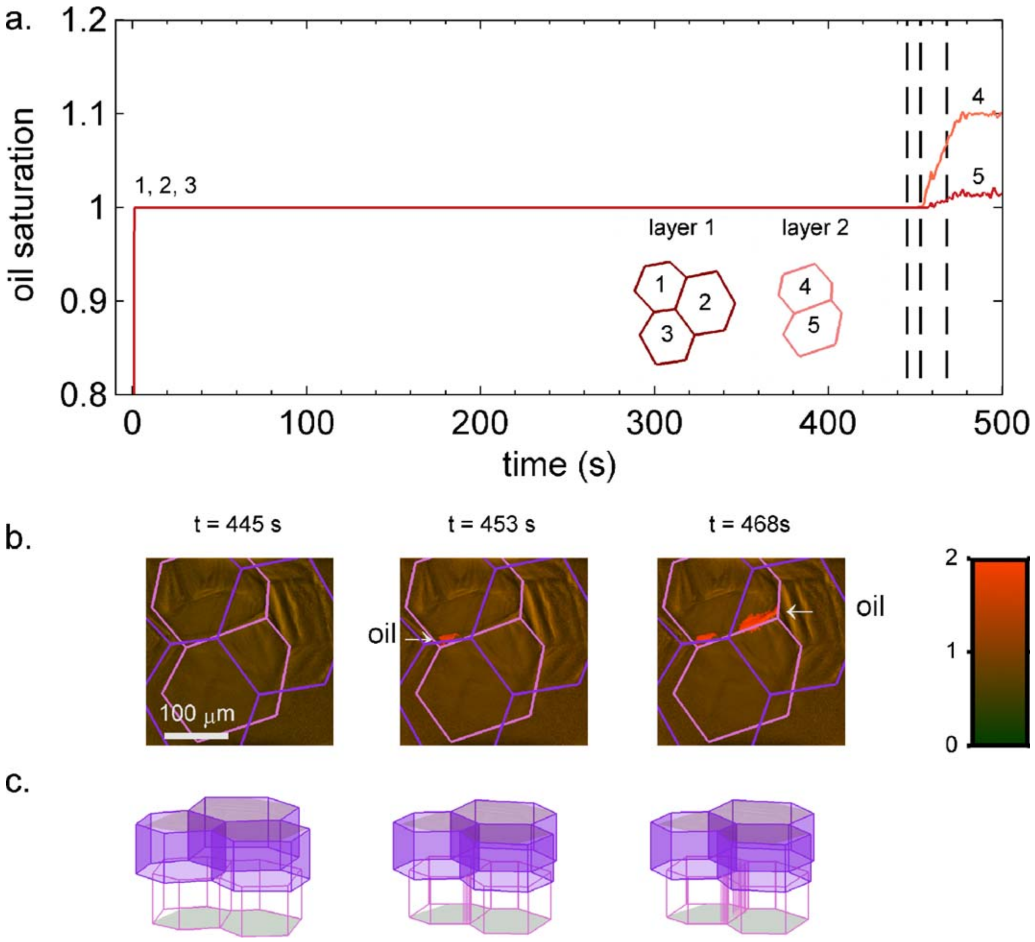

Figure 13. Identification of oil path at high magnification (×40) between two-cell layers; (a) kinetic of oil percolation between L_1 and L_2 at times t_{445}, t_{453}, and t_{468}, respectively 445, 453, and 468 s after t_0.

Images are in false colors (dark violet for L_1 filled by oil and light violet for oil percolating in L_2); (b) Composite image details, and (c) 3-D interpretation of oil percolation from L_1 to L_2. [Color figure can be viewed in the online issue, which is available at wileyonlinelibrary.com.]

pores. If the compressibility of air is assumed negligible in our experiments, air had to be evacuated to enable oil to percolate. Since the cumulated pressure gauge due to hydrostatic and capillary pressures cannot exceed 1.18 kPa in cells of diameter 80 μm (smallest cell diameter observed in our samples), the compressibility of air alone would lead to a piston incorporation of oil of 1.2% at maximum. As the cells were fully filled with oil, air needed to be removed to enable oil to fill completely the space. The coupled flows of oil and air are sketched in Figure 15 in agreement with the observations carried out.

The film of oil covering initially the first cell layer trapped an air volume. Oil flew following the walls and corners, and one or several air bubble(s) was (were) created and trapped by cell walls. The height of oil in the cut cells increased subsequently, the bubble was pushed upwards without requiring any buoyancy forces, so that similar mechanisms could be envisioned in a reverse configuration with cell on top of an oil film as studied in.[21] In shorts, an oil-air counter-current was created. Air bubbles that could be seen from the top of the sample were moving in the opposite direction of oil meniscuses, facilitated by large opening created by cutting. All these transient phenomena occurred on the time scale of few seconds maximum. The initiating driving force was gravity and capillary forces.

A similar description was assumed for the second layer but with more complications for air to escape due to small throats connecting cells. As further described in the companion paper,[16] the flow rate created by capillary forces was governed by the size of passages between L_1 and L_2. The finite compressibility of air and the possibility of air bubbles to remain trapped in convergent throats opposed the oil penetration in L_2. According to the ability of air bubbles to be fractionated and released at cell junctions, the oil flow rate appeared almost stopped. As described in similar studies,[15] bubbles could even remain indefinitely captive and prevent any additional oil penetration. In our experiments, coalescence of bubbles was more frequently observed than bubble snap-off. These observations were consistent with the higher mechanical work to split bubbles than bubble coalescence.

The necessity of an oil-air counter-current flow explains the sharp difference of behavior between the first cell layer, where oil penetrates through large openings as large as cells, and the second cell layer, where oil infiltrates through small openings created by cell injuries and cell dislocations. The main findings are summarized in Figure 15. Oil mass transfer associated to oil is governed by biphasic flows with time scales separated by one to two magnitude orders or more. The temporal heterogeneities originate from the broad distribution of defects size and from the possible presence of

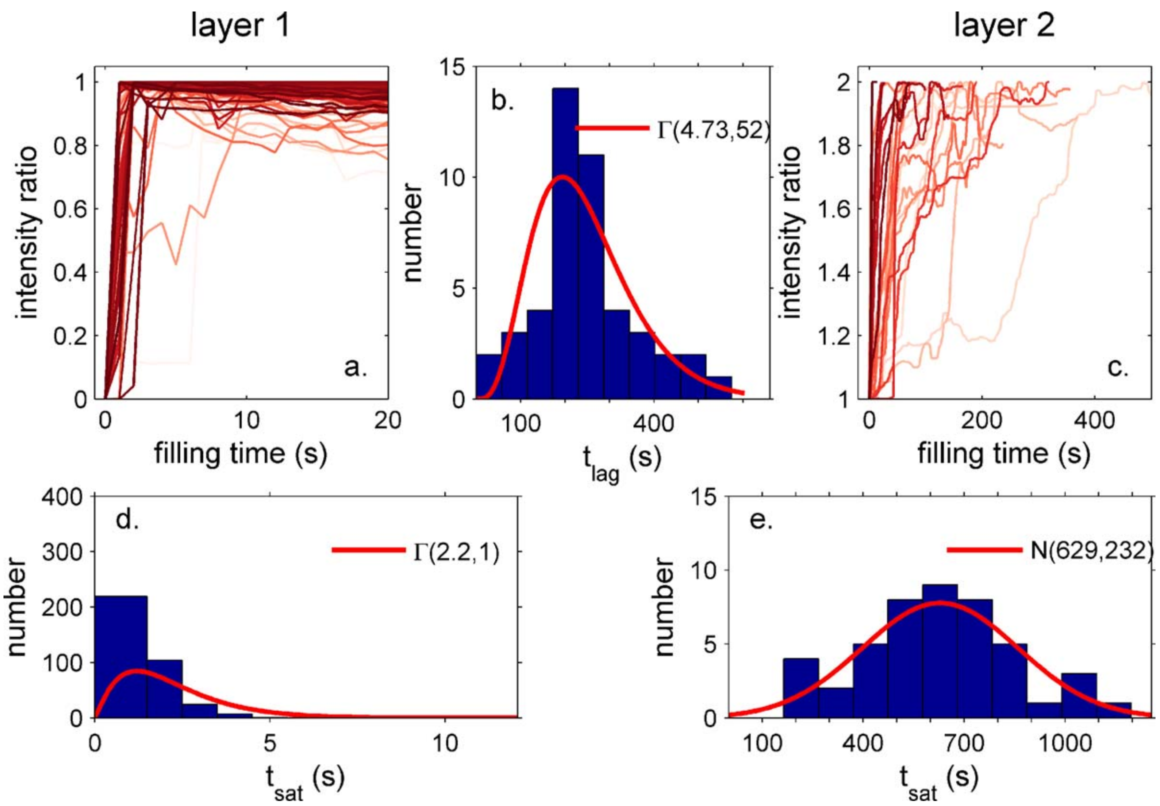

Figure 14. Kinetics of oil saturation in L_1 and L_2.

(a) Oil relative intensity in L_1 versus time; (b) Lag times calculated from Eq. 22; (c) Oil relative intensity in L_2 versus time; and (d–e) Filling times from t_0 to reach saturation of cells in L_1 and L_2, respectively. [Color figure can be viewed in the online issue, which is available at wileyonlinelibrary.com.]

trapped bubbles. It was not possible to observe directly the defects connecting cells, but it was possible to assess the amount of oil flowing through them during a prescribed time and oil-air configuration. The results are presented in Figures 8 and 9. It was particularly shown that the volumes of the spills varied over more than four decades and were highly heterogeneously distributed in the tissue plane.

Conclusions

This first study of *in situ* oil uptake has two major contributions: (1) to open new experimental routes to understand the role of cellular structure on oil uptake in fried products in postfrying conditions and (2) to bring a first evidence on the role of the incondensable phase in the slowdown of oil penetration. In this work, immersion frying was replaced advantageously by an equilibration stage with SHS. This strategy makes possible to reach thermodynamical states (temperature and relative humidity) similar to those met during frying, while enabling to control the conditions of contact with air and oil.

Two special configurations were investigated: (a) cocurrent oil-steam flow in breakthrough experiments and (b) counter-current oil-air one on a thin quartz coverslip placed on an inverted microscope. In all conditions, only spontaneous oil imbibition was enabled by preventing the condensation of steam. The results obtained in two-layer thick parenchyma tissues (free of starch) were counter-intuitive.

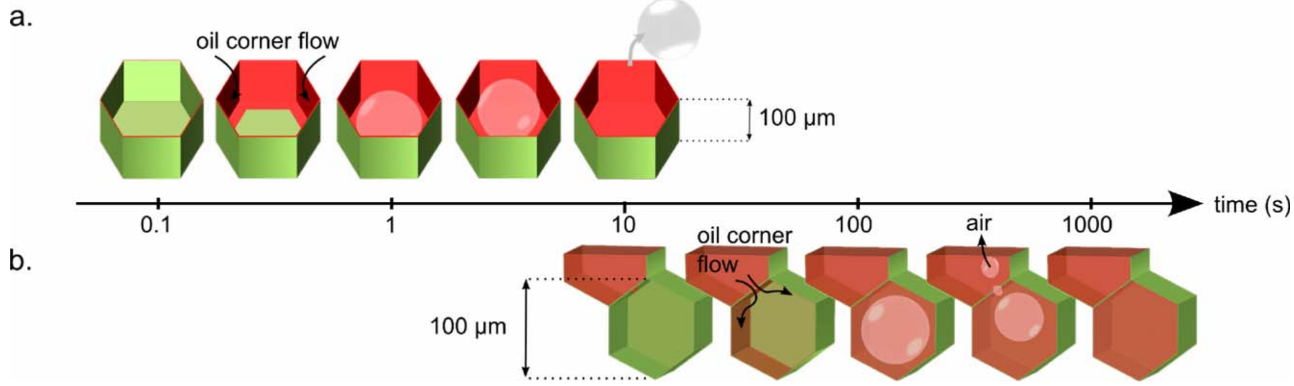

Figure 15. Interpretation of oil percolation through connected cells.

(a) L_1 (top layer) and (b) L_2 (bottom layer). [Color figure can be viewed in the online issue, which is available at wileyonlinelibrary.com.]

Only rare oil passages between cell layers were in less than 10% of cells. After 2 h of contact with oil at 120°C, breakthrough experiments showed that the median volume of single spill was lower than the volume of an intact cell. In other words, cell walls appear highly barrier to oil. A large set of microscopic observations succeeded to capture the main events controlling the penetration of oil. Smallest defects were found commensurable to plasmodesmata and have therefore a natural origin. Larger passages to oil were associated to gaps or defects between cells and were able to fill one to three cells beneath. These passages could be present in the raw material or created by the shrinkage or damage of cell walls during slicing and superheated drying.

In configurations reproducing the crust of French fries (cells open at only one end), the filling kinetics of the second cell layer was surprisingly slow, from minutes to 1 h, whereas cells of the first cell layer were filled in less than 1 s in most of the cases. In addition, the two filling processes were not found consecutive but delayed by periods as long as filling times themselves. Our interpretation is that they result from counter-current flow configuration of oil-air flows. Air bubbles were observed restricting the passage to oil. They are thought to remain trapped for long periods at the defects between cells. These new results might have important technological consequences as they demonstrate that the deep penetration of oil into cellular tissues could be stopped by the presence of an incondensable phase replacing steam. Strong oil reduction could be therefore expected by reducing dramatically the open porosity of cells of the first cell layer and by facilitating the incorporation of air in the other layers. In parfried products and in chips, it is also demonstrated that oil can be spontaneously redistributed inside the product during long-term storage.

From a mechanistic point of view, the presented observations and interpretations of oil-air menisci displacements are very consistent with recent results of[59] obtained during wicking experiments involving potato crusts. Oil capillary rise scales as the square root of time but its time scale deviates strongly from predictions using Lucas-Washburn or equivalent approximations. Similar deviations are recurrent in the scientific literature in cocurrent or counter-current configuration. Without being exhaustive, it includes the wetting of in sandstone,[78] in ground calcium carbonates,[64] in aluminoslicate powder and sieves,[79] paper coatings,[78] powders.[80] In all of these cases, the common explanation was the strong cross-section variation along the percolation route of the wetting phase. The broad distribution of defect sizes would also correlate with the strong spatial and temporal heterogeneities found in this study. From our observations, the concept of effective medium appears hence questionable when it is applied to oil uptake in fried products. Surface averaging can be reached for representative cross-section areas greater than several square centimeters. In the transverse direction, the asymmetry of behavior between the first and the second cell layer cannot be smoothed. Additional mechanistic interpretation of results and their generalization to tissues with a larger number of cells and arbitrary cellular damages are presented in a companion paper.[16]

Acknowledgments

The authors gratefully acknowledge the DISCO beamline team of synchrotron SOLEIL for supporting this study (Proposal 20110137) and the "Association Nationale de la Recherche et de la Technologie" (ANRT) agency for cofunding the study.

Literature Cited

1. Achir N, Vitrac O, Trystram G. Heat and mass transfer during frying. In: Sahin S, Sumunu SG, editors. *Advances in Deep-Fat Frying*. Boca-Raton: CRC Press, 2009:5–32.
2. Vitrac O, Trystram G, Raoult-Wack AL. Continuous measurement of convective heat flux during deep-frying: validation and application to inverse modeling. *J Food Eng*. 2003;60(2):111–124.
3. Lioumbas JS, Kostoglou M, Karapantsios TD. Surface water evaporation and energy components analysis during potato deep fat frying. *Food Res Int*. 2012;48(1):307–315.
4. Ares G, de Saldamando L, Giménez A, Claret A, Cunha LM, Guerrero L, de Moura AP, Oliveira DCR, Symoneaux R, Deliza R. Consumers' associations with wellbeing in a food-related context: a cross-cultural study. *Food Qual Prefer*. 2015;40(Part B):304–315. .
5. Moreira RG, Castell Perez ME, Barrufet MA. *Deep-Fat Frying: Fundamentals and Applications*. Maryland: Aspen Publishers Inc., 1999.
6. Costa RM, Oliveira FAR, Delaney O, Gekas V. Analysis of the heat transfer coefficient during potato frying. *J Food Eng*. 1999;39(3): 293–299.
7. Hubbard LJ, Farkas BE. Influence of oil temperature on convective heat transfer during immersion frying. *J Food Process Preserv*. 2000;24(2):143–162.
8. Vitrac O, Trystram G. A method for time and spatially resolved measurement of convective heat transfer coefficient (h) in complex flows. *Chem Eng Sci*. 2005;60(5):1219–1236.
9. Bouchon P, Aguilera JM, Pyle DL. Structure oil-absorption relationships during deep-fat frying. *J Food Sci*. 2003;68(9):2711–2716.
10. Moreira RG, Barrufet MA. A new approach to describe oil absorption in fried foods: a simulation study. *J Food Eng*. 1998;35(1):1–22.
11. Ufheil G, Escher F. Dynamics of oil uptake during deep-fat frying of potato slices. *Food Sci Technol-Lebensm-Wiss Technol*. 1996; 29(7):640–644.
12. Moreira RG, Sun XZ, Chen YH. Factors affecting oil uptake in tortilla chips in deep-fat frying. *J Food Eng*. 1997;31(4):485–498.
13. Vitrac O, Trystram G, Raoult-Wack AL. Deep-fat frying of food: heat and mass transfer, transformations and reactions inside the frying material. *Eur J Lipid Sci Technol*. 2000;102(8–9):529–538.
14. He D-B, Xu FEI, Hua T-C, Song X-Y. Oil absorption mechanism of fried food during cooling process. *J Food Process Eng*. 2012;36(4); 412–417.
15. Cortés P, Badillo G, Segura L, Bouchon P. Experimental evidence of water loss and oil uptake during simulated deep-fat frying using glass micromodels. *J Food Eng*. 2014;140:19–27.
16. Vauvre JM, Patsioura A, Kesteloot R, Vitrac O. Multiscale modeling of oil uptake in fried products. In press.
17. Ni H, Datta AK. Moisture, Oil and energy transport during deep-fat frying of food materials. *Food Bioprod Process*. 1999;77(3):194–204.
18. Halder A, Dhall A, Datta AK. An improved, easily implementable, porous media based model for deep-fat frying—part I: model development and input parameters. *Food Bioprod Process*. 2007;85(C3): 209–219.
19. Halder A, Dhall A, Datta AK. Modeling transport in porous media with phase change: applications to food processing. *Trans ASME*. 2011;133(3):031010(13 pages).
20. Yamsaengsung R, Moreira RG. Modeling the transport phenomena and structural changes during deep fat frying—part 1: model development. *J Food Eng*. 2002;53(1):1–10.
21. Achir N, Vitrac O, Trystram G. Direct observation of the surface structure of French fries by UV-VIS confocal laser scanning microscopy. *Food Res Int*. 2010;43(1):307–314.
22. Vauvre JM, Kesteloot R, Patsioura A, Vitrac O. Microscopic oil uptake mechanisms in fried products. *Eur J Lipid Sci Technol*. 2014; 116(6):741–755.
23. Gamble MH, Rice P. Effect of pre-fry drying of oil uptake and distribution in potato crisp manufacture. *Int J Food Sci Technol*. 1987; 22(5):535–548.
24. Farkas BE, Singh RP, Rumsey TR. Modeling heat and mass transfer in immersion frying .1. Model development. *J Food Eng*. 1996; 29(2):211–226.
25. Farkas BE, Singh RP, Rumsey TR. Modeling heat and mass transfer in immersion frying. II, model solution and verification. *J Food Eng*. 1996;29(2):227–248.

26. Vitrac O, Dufour D, Trystram G, Raoult-Wack AL. Characterization of heat and mass transfer during deep-fat frying and its effect on cassava chip quality. *J Food Eng.* 2002;53(2):161–176.
27. Achir N, Vitrac O, Trystram G. Simulation and ability to control the surface thermal history and reactions during deep fat frying. *Chem Eng Process.* 2008;47(11):1953–1967.
28. Halder A, Dhall A, Datta AK. An improved, easily implementable, porous media based model for deep-fat frying—part II: results, validation and sensitivity analysis. *Food Bioprod Process.* 2007;85(C3): 220–230.
29. Bassama J, Brat P, Bohuon P, Hocine B, Boulanger R, Guenata Z. Acrylamide kinetic in plantain during heating process: precursors and effect of water activity. *Food Res Int.* 2011;44(5):1452–1458.
30. Thussu S, Datta AK. Texture prediction during deep frying: a mechanistic approach. *J Food Eng.* 2012;108(1):111–121.
31. Saguy IS, Ufheil G, Livings S. Oil uptake in deep-fat frying: review. *OCL—Ol Corps Gras Lipides.* 1998;5(1):30–35.
32. Mehta U, Swinburn B. A review of factors affecting fat absorption in hot chips. *Crit Rev Food Sci Nutr.* 2001;41(2):133–154.
33. Dana D, Saguy IS. Review: Mechanism of oil uptake during deep-fat frying and the surfactant effect-theory and myth. *Adv Colloid Interface Sci.* 2006;128:267–272.
34. Ziaiifar AM, Achir N, Courtois F, Trezzani I, Trystram G. Review of mechanisms, conditions, and factors involved in the oil uptake phenomenon during the deep-fat frying process. *Int J Food Sci Technol.* 2008;43(8):1410–1423.
35. Farkas BE. *Modeling Immersion Frying as a Moving Boundary Problem*. Davis: University of California, 1994.
36. Sandhu J, Bansal H, Takhar PS. Experimental measurement of physical pressure in foods during frying. *J Food Eng.* 2013;115(2):272–277.
37. Dullien FAL. *Porous Media: Fluid Transport and Pore Structure*. New-York: Academic Press, 1979.
38. Kaviany M. *Principles of Heat Transfer in Porous Media*. 2nd ed. Berlin, Germany: Springer-Verlag, 1997.
39. Bouchon P, Pyle DL. Modelling oil absorption during post-frying cooling—ii: solution of the mathematical model, model testing and simulations. *Food Bioprod Process.* 2005;83(C4):261–272.
40. Pinthus EJ, Saguy IS. Initial interfacial tension and oil uptake by deep-fat fried foods. *J Food Sci.* 1994;59(4):804–807.
41. Reeve RM, Timm H, Weaver ML. Cell size in Russet Burbank potato tubers with various levels of nitrogen and soil moisture tensions. *Am Potato J.* 1971;48(12):450–456.
42. Chistyakov AD. Fugacity coefficients for water vapor. *Russ J Phys Chem.* 2007;81(4):651–653.
43. Bassal A, Vasseur J, Lebert A. Measurement of water activity above 100°C. *J Food Sci.* 1993;58(2):449–452.
44. Bassal A, Vasseur J, Loncin M. Sorption isotherms of food materials above 100°C. *Food Sci Technol-Lebensm-Wiss Technol.* 1993;26(6): 505–511.
45. Anderson RB. Modifications of the Brunauer, Emmett and Teller Equation1. *J Am Chem Soc.* 1946;68(4):686–691.
46. Boer JH. *The Dynamical Character of Adsorption*. Oxford: Clarendon Press, 1953.
47. Guggenheim EA. *Applications of Statistical Mechanics*. Oxford: Clarendon P.; 1966.
48. Quirijns EJ, van Boxtel AJB, van Loon WKP, van Straten G. Sorption isotherms, GAB parameters and isosteric heat of sorption. *J Sci Food Agric.* 2005;85(11):1805–1814.
49. Rice P, Gamble MH. Modeling moisture loss during potato slice frying. *Int J Food Sci Technol.* 1989;24(2):183–187.
50. Moyano PC, Berna AZ. Modeling water loss during frying of potato strips: effect of solute impregnation. *Dry Technol.* 2002;20(7):1303–1318.
51. Vitrac O, Dufour D, Trystram G, Raoult-Wack AL. Deep-fat frying of cassava: influence of raw material properties on chip quality. *J Sci Food Agric.* 2001;81(2):227–236.
52. Muskat M, Meres MW. The flow of heterogeneous fluids through porous media. *Physics.* 1936;7(9):346–363.
53. Warning A, Verboven P, Nicolaï B, van Dalen G, Datta AK. Computation of mass transport properties of apple and rice from X-ray microtomography images. *Innov Food Sci Emerg Technol.* 2014; 24:14–27.
54. Degruyter W, Burgisser A, Bachmann O, Malaspinas O. Synchrotron X-ray microtomography and lattice Boltzmann simulations of gas flow through volcanic pumices. *Geosphere.* 2010;6(5):470–481.
55. Feng H, Tang J, Plumb OA, Cavalieri RP. Intrinsic and relative permeability for flow of humid air in unsaturated apple tissues. *J Food Eng.* 2004;62(2):185–192.
56. Warning A, Dhall A, Mitrea D, Datta AK. Porous media based model for deep-fat vacuum frying potato chips. *J Food Eng.* 2012; 110(3):428–440.
57. Bucklet SE, Leverett MC. Mechanism of fluid displacement in sands. *Trans AIME.* 1942;146:107–116.
58. Gertz C, Klostermann S. Analysis of acrylamide and mechanisms of its formation in deep-fried products. *Eur J Lipid Sci Technol.* 2002; 104(11):762–771.
59. Kalogianni EP, Papastergiadis E. Crust pore characteristics and their development during frying of French-fries. *J Food Eng.* 2014;120: 175–182.
60. Michalski MC, Saramago BJV. Static and dynamic wetting behavior of triglycerides on solid surfaces. *J Colloid Interface Sci.* 2000; 227(2):380–389.
61. Quinchia LA, Delgado MA, Valencia C, Franco JM, Gallegos C. Viscosity Modification of high-oleic sunflower oil with polymeric additives for the design of new biolubricant formulations. *Environ Sci Technol.* 2009;43(6):2060–2065.
62. Oppenheim A, Schafer R, Stockham T. Non-linear filtering of multiplied and convolved signals. *Proc IEEE.* 1968;56:1264–1291.
63. Bromiley PA, Thacker NA, Courtney P. Non-parametric image subtraction using grey level scattergrams. *Image Vision Comput.* 2002; 20(9–10):609–617.
64. Schoelkopf J, Gane PAC, Ridgway CJ, Matthews GP. Practical observation of deviation from Lucas–Washburn scaling in porous media. *Colloids Surf A Physicochem Eng Asp.* 2002;206(1–3):445–454.
65. Fanta SW, Vanderlinden W, Abera MK, Verboven P, Karki R, Ho QT, De Feyter S, Carmeliet J, Nicolai BM. Water transport properties of artificial cell walls. *J Food Eng.* 2012;108(3):393–402.
66. Khalfaoui M, Knani S, Hachicha MA, Lamine AB. New theoretical expressions for the five adsorption type isotherms classified by BET based on statistical physics treatment. *J Colloid Interface Sci.* 2003; 263(2):350–356.
67. Al-Muhtaseb AH, McMinn WAM, Magee TRA. Water sorption isotherms of starch powders: part 1: mathematical description of experimental data. *J. Food Eng.* 2004;61(3):297–307.
68. Talja RA, Helén H, Roos YH, Jouppila K. Effect of various polyols and polyol contents on physical and mechanical properties of potato starch-based films. *Carbohydr Polym.* 2007;67(3):288–295.
69. Mauseth JD. *Plant Anatomy*. Caldwell, NJ: Blackburn Press, 2008.
70. Robards AW. Plasmodesmata. *Annu Rev Plant Physiol Plant Molec Biol.* 1975;26:13–29.
71. Fry SC. Phonolic components of the primary cell wall and their possible rôle in the hormonal regulation of growth. *Planta.* 1979;146(3): 343–351.
72. Duchartre PÉS. Éléments de botanique, comprenant l'anatomie, l'organographie, la physiologie des plantes, les familles naturelles et la géographie botanique. Paris: J.-B. Baillière, 1867.
73. Iterson GV, Jr., A.D.J. Meeuse. The shape of cells in homogeneous tissues I. *Proceed kon Akad Wetensh Amsterdam.* 1941;44:770–778.
74. Iterson Gv, Jr., A.D.J. Meeuse. The shape of cells in homogeneous tissues II. *Proceed kon Akad Wetensh Amsterdam.* 1941;44:897–906.
75. Lisinska G, Golubowska G. Structural changes of potato tissue during French fries production. *Food Chem.* 2005;93(4):681–687.
76. Hirsch LM, Thompson AH. Size-dependent scaling of capillary invasion including buoyancy and pore size distribution effects. *Phys Rev E.* 1994;50(3):2069–2086.
77. Ferer M, Bromhal GS, Smith DH. Pore-level modeling of drainage: crossover from invasion percolation fingering to compact flow. *Phys Rev E.* 2003;67(5):051601.
78. Dullien FAL, El-Sayed MS, Batra VK. Rate of capillary rise in porous media with nonuniform pores. *J Colloid Interface Sci.* 1977; 60(3):497–506.
79. Patro D, Bhattacharyya S, Jayaram V. Flow kinetics in porous ceramics: understanding with non-uniform capillary models. *J Am Ceram Soc.* 2007;90(10):3040–3046.
80. Brielles N, Chantraine F, Viana M, Chulia D, Branlard P, Rubinstenn G, Lequeux F, Lasseux D, Birot M, Roux D, Mondain-Monval O. Imbibition and dissolution of a porous medium. *Ind Eng Chem Res.* 2007;46(17):5785–5793.

Manuscript received Sep. 18, 2014, and revision received Dec. 24, 2014.